

**Table 1.** Log of the *RXTE* and OSSE observations. The *ASCA* observation, near-simultaneous with the *RXTE* observation 3, is described in Section 2.

No.	Date (1996)	Time [UT]	PCA		Time [UT]	HEXTE		Time [UT]	OSSE	
			Exposure [s]	Count rate [s <sup>-1</sup> ] (4–50 keV)		Exposure [s]	Count rate [s <sup>-1</sup> ] (15–200 keV)		Exposure <sup>a</sup> [s]	Count rate [s <sup>-1</sup> ] (50–1000 keV)
1	May 22	19:05:21–19:47:45	2176	7437±34	17:58:41–18:17:53	815	253.7±1.9			
2	May 23	14:28:17–15:05:05	1792	6929±29	14:28:33–14:53:05	1136	319.7±1.5			
3	May 30	07:57:53–08:35:29	1872	4796±22	07:57:37–08:18:25	850	163.3±1.6			
4	June 17	01:45:37–01:54:25	544	3357±17	01:45:21–01:54:57	1062	77.8±2.2	01:25:06–02:08:47	4496	8.25±0.61
5	June 17	04:57:53–05:16:17	992	5113±25	05:00:01–05:17:05	647	117.4±1.8	04:30:47–05:16:40	4598	7.52±0.63
6	June 17	08:09:53–08:42:25	816	6309±31	08:09:53–08:42:57	1061	175.1±1.7	07:47:23–09:12:52	3108	11.85±0.77
7	June 18	03:23:13–03:34:25	688	2893±15	03:22:57–03:34:41	510	65.6±2.0	02:52:42–04:04:47	2670	5.79±0.81
8	June 18	06:47:45–07:00:17	768	2859±14	06:38:41–07:01:05	709	54.0±1.9	06:04:56–07:30:08	3506	5.96±0.71
9	June 18	09:59:45–10:25:21	1360	6011±29	09:59:45–10:25:53	1140	140.9±1.6	10:00:15–10:41:46	4235	8.59±0.64
10	June 14–25							15:55:58–13:13:20 <sup>b</sup>	670501	9.833±0.098

<sup>a</sup>The sum of two individual detectors live times.

<sup>b</sup>The start and end time on June 14 and 25, respectively.

**Table 2.** The fit results of the non-thermal model to the data. Values in parenthesis denote parameters fixed during the fits. Other important fixed parameters are:  $\ell_s = 10$ ,  $\gamma_{\min} = 1.3$ ,  $i = 45^\circ$ ,  $A_{\text{Fe}} = 1.0$ . See Section 3.8 for discussion of the fitted values of  $M_X$ .

Obs.	$N_{\text{H}}$ ( $10^{21} \text{ cm}^{-2}$ )	$kT_{\text{max}}$ (eV)	$M_X$ ( $M_\odot$ )	$\ell_{\text{nth}}/\ell_{\text{h}}$	$\ell_{\text{h}}/\ell_{\text{s}}$	$\tau_i$	$\Gamma_{\text{inj}}$	$\Omega/2\pi$	$\xi$ ( $\text{erg cm s}^{-1}$ )	$E_{\text{line}}$ (keV)	EW (eV)	$\chi^2/\text{d.o.f.}$
1	(5.0)	(300)	14.7 <sup>+1.8</sup> <sub>-1.1</sub>	(1.0)	1.04 <sup>+0.16</sup> <sub>-0.21</sub>	2.35 <sup>+0.21</sup> <sub>-0.33</sub>	2.54 <sup>+0.09</sup> <sub>-0.08</sub>	0.24 <sup>+0.05</sup> <sub>-0.04</sub>	8700 <sup>+5900</sup> <sub>-5000</sub>	6.52 <sup>+0.19</sup> <sub>-0.20</sub>	150 <sup>+50</sup> <sub>-50</sub>	478.5/422
2	(5.0)	(300)	11.4 <sup>+0.7</sup> <sub>-0.7</sub>	(1.0)	1.60 <sup>+0.12</sup> <sub>-0.20</sub>	1.55 <sup>+0.10</sup> <sub>-0.16</sub>	2.61 <sup>+0.02</sup> <sub>-0.03</sub>	0.30 <sup>+0.04</sup> <sub>-0.03</sub>	780 <sup>+390</sup> <sub>-210</sub>	6.44 <sup>+0.24</sup> <sub>-0.25</sub>	120 <sup>+40</sup> <sub>-50</sub>	393.2/422
3	5.2 <sup>+0.1</sup> <sub>-0.2</sub>	350 <sup>+8</sup> <sub>-9</sub>	13.3 <sup>+1.0</sup> <sub>-0.8</sub>	0.77 <sup>+0.05</sup> <sub>-0.04</sub>	0.36 <sup>+0.01</sup> <sub>-0.02</sub>	0.25 <sup>+0.05</sup> <sub>-0.04</sub>	2.54 <sup>+0.11</sup> <sub>-0.07</sub>	0.63 <sup>+0.13</sup> <sub>-0.11</sub>	350 <sup>+250</sup> <sub>-120</sub>	6.37 <sup>+0.14</sup> <sub>-0.14</sub>	120 <sup>+50</sup> <sub>-30</sub>	618.2/574
4	(5.0)	480 <sup>+110</sup> <sub>-70</sub>	5.6 <sup>+3.9</sup> <sub>-2.7</sub>	(1.0)	0.27 <sup>+0.08</sup> <sub>-0.04</sub>	(0.25)	2.96 <sup>+0.06</sup> <sub>-0.07</sub>	0.60 <sup>+0.12</sup> <sub>-0.14</sub>	460 <sup>+2520</sup> <sub>-270</sub>	6.43 <sup>+0.19</sup> <sub>-0.21</sub>	170 <sup>+50</sup> <sub>-60</sub>	423.9/476
5	(5.0)	470 <sup>+120</sup> <sub>-60</sub>	7.0 <sup>+4.2</sup> <sub>-3.5</sub>	(1.0)	0.27 <sup>+0.08</sup> <sub>-0.04</sub>	(0.25)	3.30 <sup>+0.03</sup> <sub>-0.05</sub>	0.67 <sup>+0.11</sup> <sub>-0.10</sub>	450 <sup>+480</sup> <sub>-130</sub>	6.41 <sup>+0.20</sup> <sub>-0.21</sub>	160 <sup>+50</sup> <sub>-60</sub>	515.5/476
6	(5.0)	470 <sup>+60</sup> <sub>-30</sub>	7.4 <sup>+2.7</sup> <sub>-2.6</sub>	(1.0)	0.26 <sup>+0.04</sup> <sub>-0.02</sub>	(0.25)	3.33 <sup>+0.05</sup> <sub>-0.04</sub>	0.73 <sup>+0.09</sup> <sub>-0.09</sub>	410 <sup>+190</sup> <sub>-110</sub>	6.30 <sup>+0.22</sup> <sub>-0.10</sub>	140 <sup>+50</sup> <sub>-50</sub>	614.8/476
7	(5.0)	520 <sup>+90</sup> <sub>-50</sub>	4.0 <sup>+1.9</sup> <sub>-1.6</sub>	(1.0)	0.30 <sup>+0.07</sup> <sub>-0.06</sub>	(0.25)	2.87 <sup>+0.08</sup> <sub>-0.08</sub>	0.62 <sup>+0.13</sup> <sub>-0.13</sub>	460 <sup>+620</sup> <sub>-240</sub>	6.48 <sup>+0.08</sup> <sub>-0.18</sub>	190 <sup>+60</sup> <sub>-60</sub>	504.7/476
8	(5.0)	490 <sup>+100</sup> <sub>-60</sub>	5.0 <sup>+2.9</sup> <sub>-2.0</sub>	(1.0)	0.25 <sup>+0.08</sup> <sub>-0.05</sub>	(0.25)	2.96 <sup>+0.09</sup> <sub>-0.08</sub>	0.60 <sup>+0.14</sup> <sub>-0.08</sub>	590 <sup>+2720</sup> <sub>-280</sub>	6.49 <sup>+0.18</sup> <sub>-0.19</sub>	180 <sup>+60</sup> <sub>-30</sub>	610.2/476
9	(5.0)	440 <sup>+150</sup> <sub>-30</sub>	9.1 <sup>+3.0</sup> <sub>-5.0</sub>	(1.0)	0.26 <sup>+0.02</sup> <sub>-0.02</sub>	(0.25)	3.43 <sup>+0.05</sup> <sub>-0.02</sub>	0.67 <sup>+0.09</sup> <sub>-0.08</sub>	510 <sup>+230</sup> <sub>-60</sub>	6.40 <sup>+0.21</sup> <sub>-0.20</sub>	140 <sup>+50</sup> <sub>-50</sub>	549.5/476

# Radiation mechanisms and geometry of Cygnus X-1 in the soft state

Marek Gierliński<sup>1,2</sup>, Andrzej A. Zdziarski<sup>2</sup>, Juri Poutanen<sup>3</sup>, Paolo S. Coppi<sup>4</sup>, Ken Ebisawa<sup>5</sup> and W. Neil Johnson<sup>6</sup>

<sup>1</sup>*Astronomical Observatory, Jagiellonian University, Orla 171, 30-244 Cracow, Poland*

<sup>2</sup>*N. Copernicus Astronomical Center, Bartycka 18, 00-716 Warsaw, Poland*

<sup>3</sup>*Stockholm Observatory, SE-133 36 Saltsjöbaden, Sweden*

<sup>4</sup>*Astronomy Department, Yale University, P.O. Box 208101, New Haven, CT 062520-8101, USA*

<sup>5</sup>*Code 660.2, Laboratory for High Energy Astrophysics, NASA/Goddard Space Flight Center, Greenbelt, MD 20771, USA (also at Universities Space Research Association)*

<sup>6</sup>*E. O. Hulburt Center for Space Research, Naval Research Laboratory, Washington, DC 20375, USA*

Accepted Received

## ABSTRACT

We present X-ray/ $\gamma$ -ray spectra of Cyg X-1 observed during the transition from the hard to the soft state and in the soft state by *ASCA*, *RXTE* and *CGRO/OSSE* in 1996 May and June. The spectra consist of a dominant soft component below  $\sim 2$  keV and a power-law-like continuum extending to at least  $\sim 800$  keV. We interpret them as emission from an optically-thick, cold accretion disc and from an optically-thin, non-thermal corona above the disc. A fraction  $f \sim 0.6$  of total available power is dissipated in the corona.

We model the soft component by multi-colour blackbody disc emission taking into account the torque-free inner-boundary condition. If the disc extends down to the minimum stable orbit, the *ASCA/RXTE* data yield the most probable black hole mass of  $M_X \approx 10M_\odot$  and an accretion rate,  $\dot{M} \approx 0.5L_E/c^2$ , locating Cyg X-1 in the soft state in the upper part of the stable, gas-pressure dominated, accretion-disc solution branch.

The spectrum of the corona is well modelled by repeated Compton scattering of seed photons from the disc off electrons with a hybrid, thermal/non-thermal distribution. The electron distribution can be characterized by a Maxwellian with an equilibrium temperature of  $kT_e \sim 30\text{--}50$  keV and a Thomson optical depth of  $\tau \sim 0.3$  and a quasi-power-law tail. The compactness of the corona is  $2 \lesssim \ell_h \lesssim 7$ , and a presence of a significant population of electron-positron pairs is ruled out.

We find strong signatures of Compton reflection from a cold and ionized medium, presumably an accretion disc, with an apparent reflector solid angle,  $\Omega/2\pi \sim 0.5\text{--}0.7$ . The reflected continuum is accompanied by a broad iron  $K\alpha$  line.

**Key words:** accretion, accretion discs – radiation mechanisms: non-thermal – stars: individual (Cygnus X-1) – gamma-rays: observations – gamma-rays: theory – X-rays: stars

## 1 INTRODUCTION

Cyg X-1 is the best-studied Galactic black-hole candidate. Its X-ray source was discovered in a 1964 June rocket flight (Bowyer et al. 1965). Its optical companion is HDE 226868 (Webster & Murdin 1972; Bolton 1972), an OB supergiant (Walborn 1973). HDE 226868 belongs to the NGC 6871/Cyg OB3 association (Massey, Johnson & DeGioia-Eastwood 1995). The distance to the association has been measured

by Massey et al. (1995) to be  $D \approx 2.1 \pm 0.1$  kpc, whereas Malysheva (1997) obtained  $D \approx 1.8$  kpc using a different photometric system. Hereafter, we adopt  $D = 2$  kpc. We note that a commonly-used value of 2.5 kpc was obtained from the lower limit set by the extinction observed towards Cyg X-1 compared to the extinction–distance dependence for stars with directions close to that of Cyg X-1 (Bregman et al. 1973; Margon, Bowyer & Stone 1973). However, this method cannot be used for OB supergiants, in which case

a significant part of the extinction is commonly local (e.g. Massey et al. 1995).

The spectroscopic mass function is

$$f_M = \frac{M_X \sin^3 i}{(1 + M_O/M_X)^2} = (0.252 \pm 0.010) M_\odot \quad (1)$$

(Gies & Bolton 1982), where  $i$  is the inclination of the orbital axis to the observer,  $M_O$  and  $M_X$  are the masses of the supergiant and the compact object, respectively. The mass ratio,  $q \equiv M_O/M_X$ , has been constrained to be within  $1.5 \lesssim q \lesssim 2.3$  (Ninkov, Walker & Yang 1987; Gies & Bolton 1986). Thus,  $M_X$  is strongly anticorrelated with  $i$ ,

$$1.5 M_\odot \lesssim M_X \sin^3 i \lesssim 2.9 M_\odot. \quad (2)$$

The companion mass,  $M_O$ , is probably in a range between  $\sim 15 M_\odot$  (Herrero et al. 1995) and  $\sim 30 M_\odot$  (Gies & Bolton 1986). This mass range together with the above range of  $q$  lead to  $M_X$  between  $\sim 6.5 M_\odot$  and  $\sim 20 M_\odot$ . Combined with the mass function, these constraints imply  $25^\circ \lesssim i \lesssim 50^\circ$ . This is within limits from various considerations (e.g. Dolan & Tapia 1989; Ninkov et al. 1987; Davis & Hartman 1983) yielding  $25^\circ \leq i \leq 67^\circ$  (where the upper limit is due to the lack of eclipses), and a recent H $\alpha$  Doppler tomography (Sowers et al. 1998), giving  $i \leq 55^\circ$ .

The X-ray/ $\gamma$ -ray (hereafter X $\gamma$ ) emission of Cyg X-1 undergoes transitions between a hard (also called ‘low’) spectral state and a soft (‘high’) one. Most of the time the source is in the hard state, where the X $\gamma$  spectrum can be roughly described by a hard power law with a photon index of  $\Gamma \sim 1.6$ – $1.8$  and a high-energy cut-off above  $\sim 100$  keV, and a Compton reflection component including an Fe K $\alpha$  line (e.g. Gierliński et al. 1997a, hereafter G97). A soft excess observed below  $\sim 3$  keV includes a blackbody with temperature  $kT_{\text{bb}} \sim 0.15$  keV (Bałucińska-Church et al. 1995; Ebisawa et al. 1996). A likely model for the hard state of Cyg X-1 embodies Comptonization of blackbody photons from an optically-thick accretion disc in a hot, thermal, optically-thin plasma.

In the soft state, the X $\gamma$  spectrum is dominated by a soft, blackbody-like component peaking at  $\sim 1$  keV followed by a tail, which can be roughly described as a power law with  $\Gamma \sim 2.5$  (Dolan et al. 1977; Ogawara et al. 1982), extending to at least several hundred keV (Phlips et al. 1996). The soft component can be modelled as thermal emission from an optically-thick accretion disc (Mitsuda et al. 1984; Hanawa 1989). The nature of the hard tail has remained unclear. The soft state of Cyg X-1 was observed in 1970, 1975, 1980, 1994 and 1996, each time lasting no more than a few months (Liang & Nolan 1984; Cui et al. 1997). In 1994, the soft state was observed only in hard X-rays and soft  $\gamma$ -rays by the OSSE and BATSE detectors aboard *Compton Gamma Ray Observatory* (Phlips et al. 1996; Paciesas et al. 1997; Ling et al. 1997), with no accompanying observations in soft X-rays. Figure 1 shows X $\gamma$  spectra of Cyg X-1 in the hard and soft states of 1991 and 1996, respectively, as well as in an intermediate state of 1996 May.

In this paper, we study *RXTE*, *ASCA* and OSSE spectral data from observations of Cyg X-1 during its soft state in 1996. We find that spectra can be well described by emission of a non-thermal plasma in the vicinity of an accretion disc. We study then implications of this model for the size of the plasma and its location with respect to the disc, the

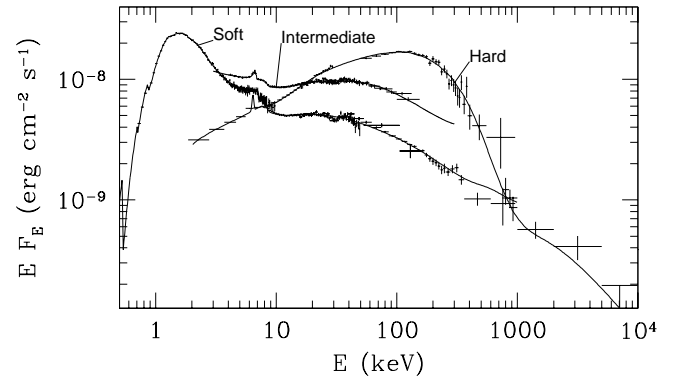


**Figure 1.** Spectral states of Cyg X-1. The hard-state spectrum was observed by *Ginga* and OSSE on 1991 June 6 (G97) and by COMPTEL 1991 May 30–June 8 (McConnell et al. 1994). The intermediate state was observed by *RXTE* on 1996 May 23 (data set 2 in Table 1). The soft state was observed by *ASCA* and *RXTE* on 1996 May 30 (data set 3) and by OSSE 1996 June 14–25 (data set 10). Here and in subsequent figures, the spectral data are rebinned for clarity. The curves correspond to the hybrid model described in Section 3.4.

presence of  $e^+e^-$  pairs, the inner radius of the accretion disc, the disc stability, and the mass of the central black hole.

## 2 THE DATA

The soft state of 1996 lasted approximately from May 16 to August 11 (Zhang et al. 1997c). The observation log of *RXTE* and OSSE observations is given in Table 1.

The *RXTE* data, from the HEASARC public archive, were obtained during observations with proposal numbers 10412 and 10512. After preliminary selection, we analysed the data of 1996 May 22, 23, 30, and June 17, 18. During the reduction, we rejected data affected by the South Atlantic Anomaly and those for which elevation above Earth’s horizon was less than  $10^\circ$ . We then constructed PCA pulse-height spectra summing up counts from all PCA layers and detectors. We obtained HEXTE spectra separately for cluster A and B. We added a 2 per cent systematic error to each PCA channel to represent residual uncertainties of calibration. Since dead-time effects of HEXTE clusters are not yet well established, we allowed free normalization of the HEXTE spectra during spectral fits. We used the PCA response matrices v3.0 as included in the FTOOLS v4.1 released on 1998 May 8, and the HEXTE response matrices of 1997 March 20.

OSSE observed Cyg X-1 on 1996 June 14–25 (viewing period 522). The lightcurve of this observation is shown in Figure 2. The flux is moderately variable, within a factor of  $\sim 2$ . The OSSE observation overlaps with 6 *RXTE* observations on June 17 and 18 (data sets 4–9). We have thus extracted 6 OSSE data sets (in the 50–1000 keV range) nearly simultaneous with the *RXTE* observations. However, in order to get better statistics, we have increased each OSSE data interval by 30 minutes on each side of the corresponding *RXTE* interval, as shown in Table 1. The OSSE data include energy-dependent systematic errors (estimated using both in-orbit and pre-launch calibration data), which

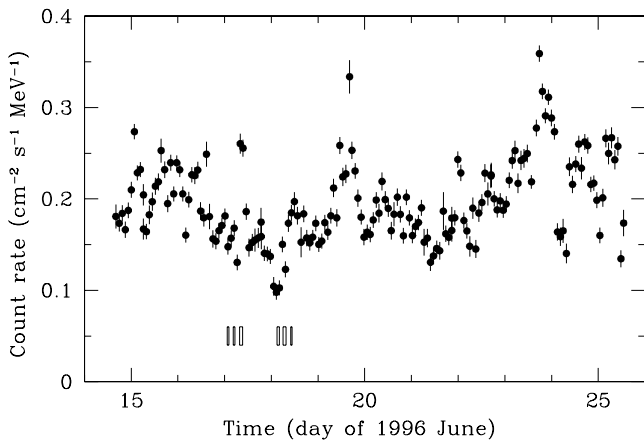


**Figure 2.** The OSSE light-curve in the 50–150 keV band. Each data point corresponds to one orbit. The boxes in the lower part of the plot indicate the times of six *RXTE* observations (Nos. 4–9 in Table 1).

range from  $\sim 3$  per cent at 50 keV to  $\sim 0.3$  per cent at  $\gtrsim 150$  keV. We have also obtained the OSSE spectrum from the entire observation (data set 10). The excellent statistics of this spectrum allows a study of the average spectral properties in soft  $\gamma$ -rays, e.g. possible presence of an annihilation feature or a high-energy cut-off.

*ASCA* observed Cyg X-1 from 1996 May 30 5<sup>h</sup>30<sup>m</sup> to May 31 3<sup>h</sup>20<sup>m</sup> UT (Dotani et al. 1997). The GIS observation was made in the standard PH mode. The SIS data suffer from heavy photon pile-up and thus are not usable. The *ASCA* and *RXTE* observations on May 30 overlap only on a short period of time. Therefore, in order to improve the statistics, we used some *ASCA* data before and after the *RXTE* observation of the data set 3, which results in 1488 s of the net exposure time (which corresponds to about 4000 s of on-source data). Although the resulting *ASCA/RXTE* data are not strictly simultaneous, the constancy of the *ASCA* light-curve, shown in Figure 3, strongly suggests constancy of the *ASCA* spectrum. We used the GIS response matrix v4.0.

Near-simultaneous *ASCA/RXTE* observations of this bright source provide us with an opportunity to study the cross-calibration of the instruments. Since the response matrices of X-ray detectors are not diagonal, we cannot compare detector counts directly. We can only choose a model spectrum, fit it to the data, and then compare the resulting spectra. For this, we use our best model (consisting of a disc blackbody and a non-thermal component) found in Section 3.5 below. We first fit the 0.7–10 keV *ASCA* data simultaneously with the 2–50 keV PCA and, in order to better establish the high-energy continuum, with the 15–200 keV HEXTE data. Figure 4a shows the data-to-model ratio for the best fit. We see that there are strong positive residuals at the high and low-energy ends of the GIS and PCA spectra, respectively, indicating that the PCA spectrum is softer than the GIS one in the range of the overlap. In particular, in the lowest-energy range of  $\sim 2.2$ –2.6 keV, the PCA channel flux exceeds the corresponding GIS flux by around 30 per cent, which corresponds to about  $12\sigma$ . This discrepancy is probably due to uncertainties in the PCA response ma-

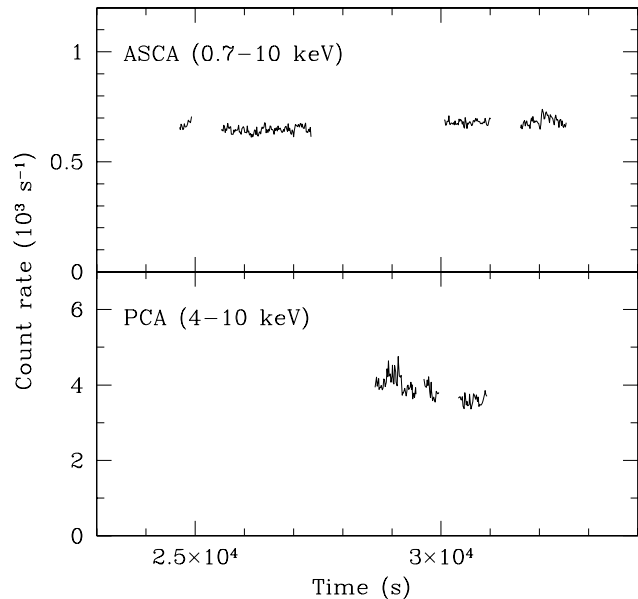


**Figure 3.** The 0.7–10 keV *ASCA*/GIS and 4–10 keV *RXTE*/PCA light-curves (time is measured from the beginning of 1996 May 30) of the nearly simultaneous observations used here (data set 3 in Table 1).

trix, especially at the lowest energies. A better agreement between the GIS and PCA data can be obtained if only the PCA channels at  $\geq 4$  keV are used, as shown in Figure 4b. Then the PCA-to-GIS flux ratios at 4–4.3 keV and 9–10 keV become 0.96 and 1.08, respectively and we use the 4–50 keV PCA data hereafter. The above uncertainty in determining the observed X-ray spectrum will then result in some systematic uncertainty in the parameters of our theoretical models.

After completion of the data fits presented in this paper, an updated version of the PCA response matrices was released as a part of *FTOOLS* v4.2 on 1998 December 10. We have then repeated the joint *ASCA*/PCA fit above with the new PCA response matrix, and found that the discrepancies reported above have remained virtually unchanged.

### 3 RESULTS

#### 3.1 Models of absorption, disc emission and reflection

For spectral fits, we use *XSPEC* v10 (Arnaud 1996). The confidence range of each model parameter is given for a 90 per cent confidence interval, i.e.,  $\Delta\chi^2 = 2.7$  (e.g. Press et al. 1992). The spectra are absorbed by the interstellar medium with a column density  $N_{\text{H}}$ , for which we use the opacities of Morrison & McCammon (1983) and the abundances of Anders & Ebihara (1982). Since only the *ASCA* data constrain  $N_{\text{H}}$  (see Table 2 below), we assume  $N_{\text{H}} = 5 \times 10^{21} \text{ cm}^{-2}$  in all fits not including the *ASCA* data.

We fit the observed spectra by a sum of 2 main primary continua. The first one is due to blackbody emission of an accretion disc. We model it using the pseudo-Newtonian (hereafter PN) potential and taking into account the torque-free

Landscape table 1 to be inserted here.

**Table 1.**

Landscape table 2 to be inserted here.

**Table 2.**

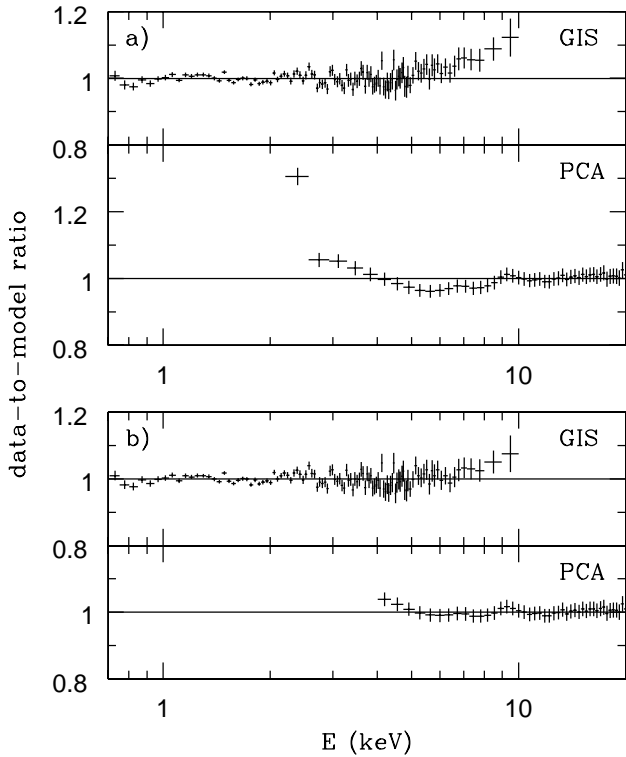


**Figure 4.** The best fit of the non-thermal model to the near-simultaneous *ASCA* and *RXTE* data of May 30 (observation 3). The upper and lower panels show the data-to-model ratios for *ASCA*/GIS and *RXTE*/PCA, respectively. (a) 0.7–20 keV residuals of the joint fit to the 0.7–10 keV *ASCA* data and the 2–50 keV PCA data. (b) The residuals to the fit with the PCA data restricted to the 4–50 keV range. Note a resulting significant improvement of the joint fit.

inner boundary condition, see Appendix A. The disc extends from an inner radius,  $R_{\text{in}}$ , corresponding to  $r_{\text{in}} \equiv R_{\text{in}}/R_{\text{g}}$  (where  $R_{\text{g}} \equiv GM/c^2$ ) to infinity, and its temperature distribution is parametrized by the maximum temperature,  $T_{\text{max}}$  reached by the disc. We assume  $r_{\text{in}} = 6$  (i.e., at the minimum stable orbit in the Schwarzschild metric) unless stated otherwise. We assume  $D = 2$  kpc and, in most fits, the disc inclination of  $i = 45^\circ$  (which is around the middle of the allowed range of  $i$ , see Section 1) and the colour-to-effective temperature ratio,  $f_{\text{col}} \equiv T_{\text{col}}/T_{\text{eff}} = 1.7$  (Shimura & Takahara 1995).

The second primary continuum corresponds to the excess emission observed above the high-energy part of the disc emission. For that continuum, we use models described in Sections 3.2–3.4. This continuum is emitted outside the disc, and thus it is Compton-reflected from the disc surface.

For modelling Compton reflection, we use viewing-angle-dependent Green’s functions of Magdziarz & Zdziarski (1995), which assume an isotropic point source (or, equivalently an optically thin corona) above a slab. However, we treat  $\Omega/2\pi$  as a free parameter, where  $\Omega$  is an effective (i.e., corresponding to the observed strength of reflection) solid angle subtended by the reflector. The reflection is accompanied by an Fe fluorescence  $K\alpha$  line centred at an energy,  $E_{\text{line}}$ . When the reflection comes from a fast rotating disc

in a strong gravitational potential, Doppler and gravitational shifts become important. We approximate these effects convolving *both* the reflected component and the Fe  $K\alpha$  line with the Schwarzschild disc line profile of Fabian et al. (1989). For simplicity, the emissivity of the reflection and of the line as a function of a disc radius is assumed to vary as  $r^{-s}$ . We expect  $s \sim 0, 2,$  and  $3$  from different parts of the disc, depending on the geometry (see Fabian et al. 1989). We assume  $s = 2$  unless stated otherwise. In calculating the relativistic distortion, we consider a range of radii from  $r_{\text{in}}$ , which equals that used for the disc blackbody emission, to  $r_{\text{out}} = 1000$ .

The reflected medium is photo-ionized, and the ionization is described by a parameter  $\xi$ . To allow direct comparison with other results, we follow Done et al. (1992) in the definition of the ionization parameter as  $\xi \equiv 4\pi F_{\text{ion}}/n$ , where  $F_{\text{ion}}$  is the 5 eV–20 keV irradiating flux in a power-law spectrum and  $n$  is the density of the reflector. (We note that in the soft state of Cyg X-1, most of the ionizing photons have energies  $\gtrsim 1$  keV, and a power-law shape of the irradiating continuum is only a rough approximation.) For simplicity, we assume that  $\xi$  is uniform in the medium. Since the ionization state of the disc close to the black hole will vary significantly with radius, the value of  $\xi$  found from the fits corresponds to an average ionization of matter at a range of radii from which most of reflection originates. The abundances in the reflector are of Anders & Ebihara (1982) except the relative Fe abundance,  $A_{\text{Fe}}$ , which is allowed to be free in some models. The ion edge energies and opacities are from Reilman & Manson (1979) except that now the Fe  $K$ -edge energies taken from Kaastra & Mewe (1993).

In our fits, we allow for free relative normalization of data from different instruments, except for the simultaneous PCA/OSSE data. In that case, we found their relative normalization is fully consistent with unity.

### 3.2 Phenomenological description

As illustrated on Figure 1, the  $X\gamma$  spectrum of Cyg X-1 in the soft state consists of a blackbody-like soft component dominant below  $\sim 2$  keV and a power-law tail extending to at least several hundred keV. In order to allow a comparison with previous results (Dotani et al. 1997, Zhang et al. 1997b) as well as to establish a phenomenological description of the spectral data, we start our analysis with a simple model consisting of a PN disc and a power law with its corresponding Compton-reflection continuum and an Fe line computed taking into account the relativistic smearing. First, we fit the simultaneous *RXTE*/OSSE data of June 17 and 18 (data sets 4–9). The photon spectral index,  $\Gamma$ , varies between about 2.3 and 2.5, which confirms the results of simultaneous ASM and BATSE monitoring of Cyg X-1 (Zhang et al. 1997b). The reflector solid angle,  $\Omega/2\pi$ , is  $\sim 0.6$ – $0.7$ , and  $\chi^2_{\nu} \sim 500/475$ .

Next, we test the *RXTE*/OSSE data for a presence of a high-energy cut-off. We multiply the power law by an exponential factor with an e-folding energy,  $E_{\text{f}}$ . Since the simultaneous *RXTE*/OSSE observations constrain  $E_{\text{f}}$  only weakly, we test the properties of the high-energy tail using the OSSE data integrated over the whole viewing period 522 (data set 10), which spectrum is detected up to  $\sim 800$  keV (Figure 5). When we fit together the *RXTE* data No. 5 and the inte-

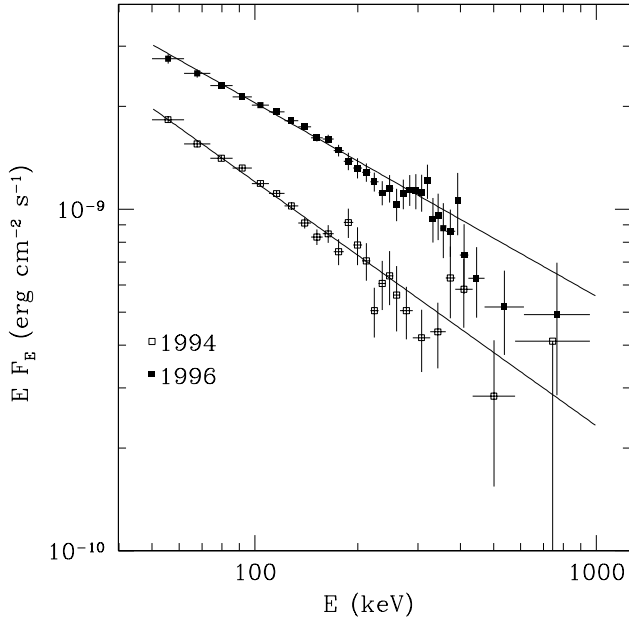


**Figure 5.** OSSE spectra of Cyg X-1 in the soft state of 1994 February (open boxes) and 1996 June (filled boxes). The former data come from the OSSE viewing period 318, 1994 February 1–8 (Phlips et al. 1996). The latter data are described in Table 1, observation 10. The two data sets are fitted by a power law with  $\Gamma = 2.72^{+0.03}_{-0.04}$ , and  $\Gamma = 2.57^{+0.02}_{-0.03}$ , respectively (solid lines).

grated OSSE spectrum, the best-fit e-folding energy is very high,  $E_f = 940^{+800}_{-310}$  keV.

On the other hand, a power law hard continuum fails to reproduce the low-energy spectrum of the simultaneous *ASCA/RXTE* observation, which was pointed out by Gierliński et al. (1997b) and C98. A fit of a model consisting of a blackbody disc, a power law and the corresponding reflection continuum with an Fe K $\alpha$  line provides a very poor fit to this data set, with  $\chi^2_\nu \sim 1100/576$ . A much better fit, with  $\chi^2_\nu = 608/574$ , can be obtained with a broken power-law continuum instead of a single power law. We find the power-law indices,  $\Gamma_1 = 2.67^{+0.02}_{-0.03}$ ,  $\Gamma_2 = 2.19 \pm 0.02$ , the break energy,  $E_{\text{break}} = (10.9 \pm 0.5)$  keV,  $\Omega/2\pi = 0.48^{+0.09}_{-0.08}$ ,  $N_{\text{H}} = (5.8 \pm 0.1) \times 10^{21}$  cm $^{-2}$ ,  $kT_{\text{max}} = 372^{+5}_{-7}$  eV,  $M_{\text{X}} = 9.4^{+0.4}_{-0.2} M_{\odot}$ ,  $\xi = (2000 \pm 600)$  erg cm s $^{-1}$ ,  $E_{\text{line}} = 6.38^{+0.16}_{-0.15}$  keV, and the line equivalent width,  $\text{EW} \approx 110$  eV. These results are relatively similar to those of Dotani et al. (1997) and C98.

Furthermore, we stress that if the tail beyond the disc blackbody is due to Comptonization of the disc blackbody photons (as it is most likely the case in Cyg X-1), the tail spectrum would have a sharp low-energy cut-off at  $\lesssim 2$  keV. A proper description of the tail is then essential for determining the disc parameters. Using of a continuum without an intrinsic low-energy cut-off (e.g. a power law) can result in an erroneous determination of the disc properties and  $N_{\text{H}}$ .

### 3.3 Thermal plasma model

As shown in the previous section, the high-energy power law in the soft state extends to very high energies ( $E_f \gtrsim 600$

keV). This contrasts the hard state, where the power law is cut off above  $\sim 100$  keV. If this spectrum were emitted by Comptonization of soft photons in a thermal plasma, the electrons would have to have a temperature of at least several hundreds keV. Then, in order to account for the observed power-law slope, the optical depth of the electrons would have to be very low,  $\lesssim 0.01$ . Subsequent scattering events in a plasma with such very low optical depth would form distinct humps in the emerging spectrum, which are clearly not seen in the data. We confirm this using a thermal-Comptonization model of Coppi (1992), assuming that seed photons for Compton up-scattering are those emitted by the disc. This model (together with a disc, reflection and a line) fitted to the *RXTE/OSSE* spectra (data sets 4–9) yields unacceptable values of  $\chi^2_\nu \sim 1000/476$ , much worse than that obtained in section 3.2 with a power-law incident continuum.

Furthermore, we find that the thermal-Comptonization model provides a very poor fit to the *ASCA/RXTE* data, as it is unable to reproduce the broken power-law shape of the tail. This result agrees with that of Cui et al. (1998, hereafter C98) who could fit those data with thermal Comptonization only assuming that the temperature of seed photons is much higher than that of the observed disc photons. Thus, we rule out the thermal Comptonization as a model for the continuum emission in the soft state of Cyg X-1.

### 3.4 Hybrid thermal/non-thermal plasma model

Since the high-energy tail in the spectrum cannot be due to emission from a thermal plasma, we fit the data using a non-thermal model of Coppi (1992) with some modifications (see also Coppi & Blandford 1992; Zdziarski, Coppi & Lamb 1990; Zdziarski, Lightman & Maciołek-Niedźwiecki 1993 and a recent review by Coppi 1999). This model embodies Compton scattering,  $e^\pm$  pair production and annihilation,  $pe^\pm$  and  $e^\pm e^\pm$  thermal and non-thermal bremsstrahlung, and energy exchange between thermal and non-thermal parts of the  $e^\pm$  distribution via Coulomb scattering. The seed photons for Compton scattering are those emitted by the PN disc. Selected  $e^-$  are accelerated to suprathermal energies and the thermal part of the  $e^\pm$  distribution can be additionally heated (apart from Compton heating/cooling and Coulomb heating by the non-thermal  $e^\pm$ ). [A similar, thermal/non-thermal, model was used, e.g., by Holman & Benka (1992) for solar flares.]

This model assumes a spherical plasma cloud with isotropic and homogeneous distributions of photons and  $e^\pm$ , and soft seed photons produced uniformly within the plasma (Coppi 1992). The properties of the plasma depend on its compactness,  $\ell \equiv \mathcal{L}\sigma_{\text{T}}/(\mathcal{R}m_e c^3)$ , where  $\mathcal{L}$  is a power of the source,  $\mathcal{R}$  is the radius of the sphere and  $\sigma_{\text{T}}$  is the Thomson cross section. We specifically use a hard compactness,  $\ell_{\text{h}}$ , which corresponds to the power supplied to the electrons, and a soft compactness,  $\ell_{\text{s}}$ , corresponding to the power supplied in the form of soft seed photons. We assume  $\mathcal{R} = 10^8$  cm, but this value is important only for bremsstrahlung emission (which is negligible in our case), and for the Coulomb logarithm (see Section 4.2 below).

This spherical model is certainly an idealization of the hot plasma source in Cyg X-1, and we need to relate the model parameters to those corresponding to the actual X $\gamma$  source in Cyg X-1. Based on the strength of the blackbody

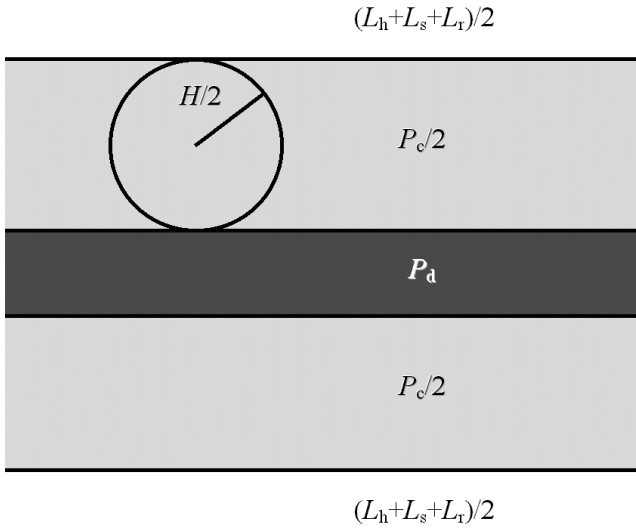


**Figure 6.** A sketch of the disc-corona geometry. The emission of the spherical plasma model is identified with that of the spherical region shown here. Power dissipated in the disc and corona are  $P_d$  and  $P_c$ , respectively.  $L_s$ ,  $L_h$ ,  $L_r$  are soft, hard and reflected luminosities, respectively. See Section 3.4 and Appendix B.

and reflection components (Section 3.2), our preferred geometry is that of a hot corona above the surface of an accretion disc. Similar to a method of Björnsson & Svensson (1991), we consider a local spherical volume with a radius  $\mathcal{R} = H/2$  inside the corona, where  $H$  is the corona scale-height, as shown in Figure 6. In some models, we will also allow the corona to cover the disc at  $R \leq R_h$  partially with the covering fraction,  $g$  ( $\leq 1$ ).

We then consider the relation of the compactnesses,  $\ell_h$  and  $\ell_s$ , obtained from fitting the spherical model, to the parameters of the corona: the luminosity in scattered photons,  $L_h$ , the luminosity in unscattered blackbody photons,  $L_s$ , the characteristic radius of the corona,  $R_h$ , and  $H$ . This will allow us to constrain the last two quantities by the observed fluxes and fits of the model. For that purpose only, we assume that the corona radiates isotropically and neglect corrections due to the finite Thomson optical depth of the corona, the finite disc albedo,  $a$ , and the viewing angle of  $i \neq 60^\circ$  (in which case the anisotropy of the blackbody flux emitted by the disc plays a role). However, we do take into account those corrections later in considering the energy balance between the disc and the corona (Section 3.9 and Appendix B).

We point out here one significant difference between the spherical and disc-corona geometries. Namely, the sphere radiates away *all* of the power supplied to the electrons as well as that supplied as seed photons. On the other hand, the isotropic corona luminosity,  $L_h$ , corresponds to only *half* of the total coronal power,  $2L_h$  (while the other half is radiated towards the disc and absorbed), whereas the disc luminosity,  $L_s$ , corresponds to all of the power in soft photons emitted by the disc. In our model fitting, we fit observed fluxes in soft and hard photons. Therefore, we have to define  $\ell_h$  in terms of the hard power radiated away (rather than the dissipated) by electrons in the spherical volume. This yields

$$\ell_h \approx \frac{1}{6g} \frac{L_h \sigma_T}{R_h m_e c^3} \frac{H}{R_h}. \quad (3)$$

We note that the numerical factor in this equation is not precise due to the approximations described above, which will introduce some systematic uncertainty in our determination of plasma parameters.

In models in this Section, we assume  $g = 1$ , which corresponds to all the blackbody photons passing through the plasma. Then, the soft compactness,  $\ell_s$ , is to be defined in the same manner as in equation (3) except that  $L_h$  is replaced by  $L_s$ . If  $g < 1$ , we will distinguish between the soft compactness in photons incident on the hot plasma and that in soft photons freely escaping (Section 3.9).

The compactnesses corresponding to the electron acceleration and to the additional heating of the thermal part of the  $e^\pm$  distribution are denoted as  $\ell_{\text{nth}}$  and  $\ell_{\text{th}}$ , respectively, and  $\ell_h = \ell_{\text{nth}} + \ell_{\text{th}}$ . In our fits, we use the ratio of  $\ell_{\text{nth}}/\ell_h$  as a parameter. The rate at which non-thermal electrons appear in the source is assumed to be a power law,  $\dot{N}_{\text{inj}}(\gamma) \propto \gamma^{-\Gamma_{\text{inj}}}$ , between the Lorentz factors of  $\gamma_{\text{min}}$  and  $\gamma_{\text{max}}$ . We hereafter assume  $\gamma_{\text{min}} = 1.3$  and  $\gamma_{\text{max}} = 1000$ . A different choice of  $\gamma_{\text{max}}$  has a negligible effect on our results as long as  $\gamma_{\text{max}} \gg \gamma_{\text{min}}$  since most of the power in the case of  $\Gamma_{\text{inj}} > 2$  (see Table 2) is injected around  $\gamma_{\text{min}}$ . The effect of the choice of  $\gamma_{\text{min}}$  on our results is discussed in Section 4.2.

The injected electrons and pairs produced in photon-photon collisions lose energy by inverse-Compton scattering (at a rate of  $\dot{\gamma}_{\text{Compton}} \propto \gamma^2$ ), so the equilibrium  $e^\pm$  distribution is *softer* than that of injected electrons. This can be seen from the steady-state continuity equation,

$$\frac{d}{d\gamma} [\dot{\gamma} N_e(\gamma)] = \dot{N}_{\text{inj}}(\gamma), \quad (4)$$

which solution leads to the non-thermal component of  $e^\pm$  distribution,  $N_e(\gamma) \propto \gamma^{-(\Gamma_{\text{inj}}+1)}$ . Therefore, the single scattering of seed photons off these  $e^\pm$  forms a power-law spectrum with photon index  $\Gamma \approx \Gamma_{\text{inj}}/2 + 1$ . In steady state, the non-thermal and thermal  $e^\pm$  have optical depths,  $\tau_{\text{nth}}$  (typically  $\ll 1$ ) and  $\tau_{\text{th}}$ , respectively, following from balance of acceleration, pair production, and energy losses. The total optical depth is denoted by  $\tau$ .

The optical depth of the thermal component,  $\tau_{\text{th}}$  (typically  $\gg \tau_{\text{nth}}$ ), is a sum of the optical depth to scattering on  $e^+e^-$  pairs and on  $e^-$  coming from ionization of atoms,  $\tau_i$ . The latter one is a free parameter of the model, but  $\tau_{\text{th}}$  as well as the equilibrium temperature of the thermal component,  $T_e$ , are computed self-consistently.

The spectrum of the model is then used to compute the corresponding continuum from Compton reflection including relativistic smearing (Section 3.1). We find that the plasma in the source is so energetic that a single Compton scattering effectively removes a Compton-reflected photon from the reflection spectrum. Then,  $\Omega/2\pi$  obtained from the fit corresponds to the unscattered part of Compton reflection.

A sequence of model spectra for varying compactness is presented on Figure 7. For parameters consistent with the observations (as found in Section 3.5 below) the spectrum is basically a power law without a break up to  $\sim 10^4$  keV. The power law is formed by a single inverse-Compton scattering of disc seed photons off the non-thermal  $e^\pm$  with optical thickness of  $\tau_{\text{nth}} \sim 10^{-2}$ . At low energies, we see the spec-



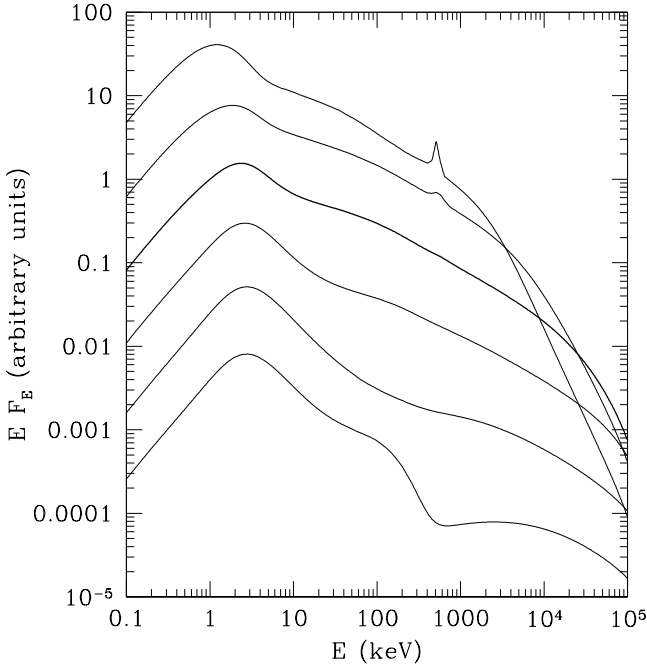


**Figure 7.** Model spectra from non-thermal plasmas above the surface of an accretion disc calculated for varying soft compactness,  $\ell_s$ . From bottom to top,  $\ell_s = 0.01, 0.1, 1, 10, 100$  and  $1000$ . Other parameters are  $\ell_h/\ell_s = 0.3$ ,  $\ell_{\text{nth}}/\ell_h = 0.9$ ,  $\tau_i = 0.3$ ,  $\Gamma_{\text{inj}} = 3$ ,  $\gamma_{\text{min}} = 1.3$ ,  $kT_{\text{max}} = 0.4$  keV. At low and high compactness, we see distortions of the hard spectrum due to Coulomb interactions (see Section 4.2) and  $e^+e^-$  pair production and annihilation (see Section 3.6), respectively. Compton reflection and seed photons escaping from the plasma without a scattering are not included in the spectra shown. The normalization of each spectrum is arbitrary.

trum of disc photons repeatedly scattered off the thermal  $e^\pm$ , as well as singly-scattered off the nonthermal  $e^\pm$ . The former scattering dominates, forming a tail beyond the disc blackbody energies, crossing the non-thermal power law at  $\sim 10$  keV.

### 3.5 Spectral fits with the hybrid model

In fitting the data, we have found we cannot uniquely determine the overall level of the compactness, which, in our fits, is given by the value of  $\ell_s$ . The joint constraints from both the *ASCA/RXTE* and *RXTE/OSSE* data yield  $5 \lesssim \ell_s \lesssim 20$ . Since the ratio of  $\ell_h/\ell_s = 0.36^{+0.01}_{-0.02}$  is well established (see below), this corresponds to constraints on the hard compactness,  $2 \lesssim \ell_h \lesssim 7$ . The upper limit is due to the onset of efficient  $e^+e^-$  pair production at  $\ell_h \gtrsim 7$  (see Figure 7), whereas the data do not show any signatures of the presence of pairs (see Section 3.6). The lower limit is due to Coulomb cooling of non-thermal electrons becoming important at low compactness (see Figure 7). At small  $\ell_h$  this process thermalizes efficiently the non-thermal electrons below some Lorentz factor (see Section 4.2), whereas the data are consistent with a non-thermal distribution close to a power law. We hereafter assume  $\ell_s = 10$  in most of fits below, and use  $\ell_h/\ell_s$  rather than  $\ell_h$  as a free parameter.

We start spectral fitting with the June 17–18

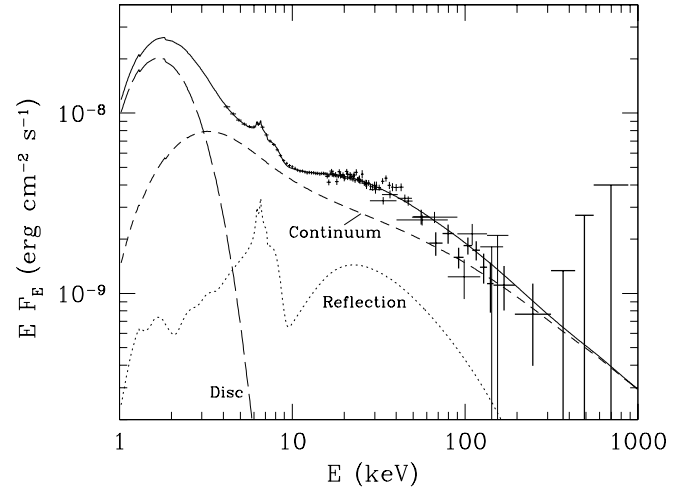


**Figure 8.** The simultaneous *RXTE* and *OSSE* observation of Cyg X-1 in the soft state on 1996 June 17 (observation No. 5) together with a model with  $\tau_i = 0.25$  (solid curve; fit parameters given in Table 2). The model is decomposed into the hot-plasma emission (short dashes), Compton reflection including the Fe K $\alpha$  line (dots), and the disc blackbody emission (long dashes).

*RXTE/OSSE* data (observations 4–9). We find that the data do not allow us to determine  $\tau_i$ . There are several shallow local minima of  $\chi^2$  in a wide range of  $\tau_i$  between  $\sim 0.2$  and  $\sim 3$ . However, models with different values of  $\tau_i$  differ significantly from each other below 4 keV, where we have no data. We find a strong correlation between  $\tau_i$  and  $\ell_h/\ell_s$ , which latter parameter is also poorly determined by the data. Therefore, in order to determine  $\tau_i$  and  $\ell_h/\ell_s$ , we use the *ASCA/RXTE* observation, for which we obtain  $\tau_i = 0.25^{+0.05}_{-0.04}$  and  $\ell_h/\ell_s = 0.36^{+0.01}_{-0.02}$  (see below). Since the spectral properties did not change significantly between 1996 May 30 and June 17–18, we assume that  $\tau_i$  also remained similar, and we fix  $\tau_i = 0.25$  in subsequent fits to the data sets 4–9. Figure 8 shows the data set 5 fitted with  $\tau_i = 0.25$ . We further note that a large value of  $\tau_i$ , e.g. 2.5, would be difficult to reconcile within the coronal model, which we find below the most likely, with the presence of strong Compton reflection in the spectrum.

For the data sets 4–9, we find the best-fitting values of  $\ell_{\text{nth}}/\ell_h \sim 0.95$ –1 and corresponding 90 per cent confidence intervals covering the range of  $\sim 0.8$ –1. Thus, in order not to introduce unnecessary free parameters, we assume  $\ell_{\text{nth}}/\ell_h = 1$  in our fits to the *RXTE/OSSE* data (see Table 2).

Subsequently, we study the *ASCA/RXTE* data of May 30. The 0.7–10 keV energy range of the GIS data allows us to determine the  $N_{\text{H}}$ , and therefore we let it free in this fit. The low-energy coverage also allows us to better constrain the direct heating of thermal electrons, and thus we let  $\ell_{\text{nth}}/\ell_h$  to be free. The fit results are shown in Table 2. The best-fitting parameters correspond to  $\tau_{\text{th}} \approx 0.26$ ,  $kT_e \approx 46$  keV, and  $\tau_{\text{nth}} \sim 10^{-2}$ . We find now the relative non-thermal power of  $\ell_{\text{nth}}/\ell_h = 0.77^{+0.05}_{-0.04}$ , which, although somewhat less than unity, still confirms our conclusion that the direct thermal heating in Cyg X-1 in the soft state is weak compared to non-thermal acceleration. The above range of  $\ell_{\text{nth}}/\ell_h$  is still consistent with the results of June 17–18 *RXTE/OSSE* fits

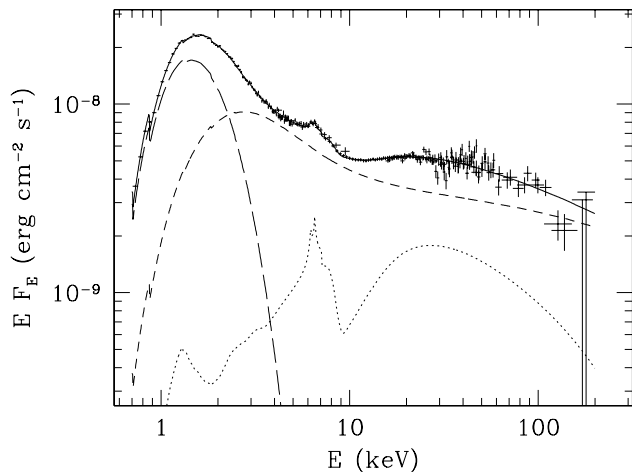


**Figure 9.** The simultaneous *ASCA* and *RXTE* observation of Cyg X-1 in the soft state on 1996 May 30 (observation No. 3). The short dashes, dots and long dashes show the Comptonization continuum, the component reflected from the cold disc and the disc emission, respectively. The solid curve shows the sum. The fit parameters are given in Table 2. The Comptonization continuum is dominated by thermal and non-thermal scattering below and above, respectively,  $\sim 15$  keV, with the resulting spectral break at that energy.

within the error bars, and thus we are not able to conclude whether the relative fraction of non-thermal power changed between May 30 and June 17–18 or not. The range of  $\ell_s$  found above corresponds, at the fitted  $\ell_h/\ell_s = 0.36^{+0.01}_{-0.02}$ , to the total compactness,  $\ell = \ell_s + \ell_h$ , of  $7 \lesssim \ell \lesssim 27$ .

We note here that the actual value of  $\ell_{\text{nth}}/\ell_h$  depends somewhat on the assumed value of  $\ell_s$ . This effect can be understood based on results of Section 4.2 below. Namely, the importance of Coulomb heating of the thermal  $e^\pm$  plasma component by non-thermal electrons decreases with increasing compactness. Thus, more direct heating of the thermal  $e^\pm$  is required at a higher compactness than at a lower one. Indeed, for the lower and upper limit of  $\ell_s$  allowable by the data, 5 and 20, we find  $\ell_{\text{nth}}/\ell_h = 0.88^{+0.08}_{-0.05}$  and  $0.72^{+0.03}_{-0.02}$ , respectively.

On 1996 May 22–23 (data sets 1 and 2), Cyg X-1 was in an intermediate state. The hard X-ray flux was significantly stronger than in soft-state observations of May 30 and June 17–18, but weaker than in the hard state (see Figure 1). Although Cyg X-1 was observed during this period only by *RXTE*, we find that the shape of the spectrum allows a determination of  $\tau_1$ . Fit results are given in Table 2. Since the soft component is relatively weak (see Figure 1), we can only constrain the seed photon temperature,  $kT_{\text{max}}$ , to be  $\lesssim 0.4$  keV, and we thus assume  $kT_{\text{max}} = 0.3$  keV. We caution here that  $kT_{\text{max}}$  is strongly anti-correlated with  $R_{\text{in}}$ . For example, the data set 1 at  $kT_{\text{max}} = 0.15$  keV yields  $R_{\text{in}}$  about 6 times larger than that for  $kT_{\text{max}} = 0.3$  keV. We also obtain the compactness ratio of  $\ell_h/\ell_s \sim 1$ , which indeed places these data between the hard and soft states, for which  $\ell_h/\ell_s \sim 10$  and 0.3–0.4, respectively.

Summarizing our results so far, we have found a satisfactory physical description of the data by a model with the main component due to Compton scattering of soft photons

from an optically-thick accretion disc in an optically thin, hot, plasma. We find the plasma cannot be purely thermal. Rather, the electrons in the plasma have a hybrid distribution with a Maxwellian component at a  $kT_e \sim 40$ –50 keV and a quasi power-law, non-thermal, tail.

### 3.6 $e^+e^-$ pairs

The optical depth of the thermal part of the  $e^\pm$  distribution,  $\tau_{\text{th}}$ , includes contributions from both ionization electrons ( $= \tau_1$ ) and  $e^+e^-$  pairs. We find first that the *ASCA/RXTE* observation (data set 3) cannot constrain the presence of pairs. Fits with  $\ell_s = 40$  and 10 with a  $\chi^2$  difference of only 2.2 yield  $\tau_{\text{th}}/\tau_1 \gg 1$  (a pair-dominated plasma) and 1.07 (an  $e^-$  dominated plasma), respectively. This is because a presence of pairs manifests itself primarily by an annihilation feature around 511 keV (see Section 4.2), which energy range is not covered by *RXTE*.

On the other hand, the *RXTE/OSSE* observations (data sets 4–9) do not constrain  $\tau_1$ , as discussed in Section 3.5 above, which again prevents us from constraining  $\tau_{\text{th}}/\tau_1$ . Therefore, we fit the *ASCA/RXTE* data set 3 together with the average *OSSE* spectrum (data set 10). The presence of pairs is now excluded at a high statistical significance. At  $\ell_s = 10$ ,  $\tau_{\text{th}}/\tau_1 \approx 1$ , and at  $\ell_s = 40$ , which yields  $\tau_{\text{th}}/\tau_1 \approx 1.4$ ,  $\chi^2$  becomes significantly worse,  $\Delta\chi^2 = +16$  at 626 d.o.f. The plasma becomes pair-dominated,  $\tau_{\text{th}}/\tau_1 \gg 1$ , at  $\ell_s = 60$ , but then  $\Delta\chi^2 = +20$ . The main contribution to the increasing  $\chi^2$  comes from the *OSSE* channels around  $m_e c^2$  due to an annihilation feature produced by the model but not present in the data. Thus, pairs appear to be negligible.

In our plasma model, we have assumed so far that the accelerated (or injected) particles are electrons rather than  $e^+e^-$  pairs (and the acceleration rate is balanced by the rate at which electrons move from the non-thermal distribution to the thermal one). On the other hand, some physical mechanisms may give rise to production of non-thermal pairs rather than electrons, as well as mostly pairs would be accelerated out of the thermal distribution if that is already pair-dominated. To investigate that case, we have considered a plasma model with an injection of  $e^+e^-$  pairs. However, this model gives an extremely poor fit to the data,  $\chi^2_\nu \sim 1000/626$ . This is due to the luminosity from annihilation of the injected pairs, which equals

$$L_{\text{annihilation}} \approx \frac{\Gamma_{\text{inj}} - 2}{(\Gamma_{\text{inj}} - 1)\gamma_{\text{min}}} L_h. \quad (5)$$

The annihilation luminosity is then large in our case with  $\Gamma_{\text{inj}} \sim 2.5$  (Table 2) and  $\gamma_{\text{min}}$  constrained to be  $\sim 1$  (see Section 4.2 below), which is in strong disagreement with the *OSSE* data showing no pair annihilation feature. Summarizing, the presence of a substantial number  $e^+e^-$  pairs in the  $X\gamma$  source of Cyg X-1 in the soft state is ruled out.

### 3.7 Compton reflection and Fe K $\alpha$ line

We find manifest signatures of reprocessing by a cold medium – an Fe K edge with a K $\alpha$  line and a broad excess over the continuum at  $\sim 10$ –100 keV – in all our data sets. The most straightforward interpretation of those features is in terms of Compton reflection of the hot-plasma emission

by an ionized, optically-thick, accretion disc. The statistical significance of the presence of reflection is very high. Fits to the data sets 3–9 without reflection are much worse,  $\chi^2_\nu \sim 2$ , than those including reflection (see Table 2), and the main cause of the bad fit are strong residuals around the Fe edge/line energies. The intermediate-state *RXTE* data sets, 1–2, are somewhat less sensitive to reflection. Still, fits without reflection are much worse ( $\chi^2 = 654$  and 586 at 425 d.o.f.) than those in Table 2.

Below, we use the simultaneous *ASCA/RXTE* observation (data set 3), which allows the most detailed study of Compton reflection and the associated  $K\alpha$  fluorescence. This is due to a broad energy range,  $\sim 0.7$ –100 keV, together with good sensitivity near 7 keV. First, we confirm that the reflected continuum is accompanied by an iron  $K\alpha$  line, by means of the standard  $F$ -test (e.g. Mises 1964). We apply here our best model (see Table 2) with relativistic Compton reflection with a line (described in Section 3.1) and without it. Our null hypothesis is that a model with the line fits the data better than a model without it. A fit without the line yields  $\chi^2_1 = 652$  with  $\nu_1 = 576$  d.o.f., whereas a fit with the line yields  $\chi^2_2 = 618$ ,  $\nu_2 = 574$  d.o.f. The chance function,  $F_m = (\Delta\chi^2/\Delta\nu)/(\chi^2_2/\nu_2)$  has a Snedecor’s  $F$  distribution. The significance level,  $P(F > F_m)$ , is the probability of committing an error of first kind, i.e. rejecting the correct hypothesis. For the fits above,  $F_m = 15.6$  and  $P(F > F_m) = 2.5 \times 10^{-7}$ , which represents a very high statistical significance that an Fe  $K\alpha$  line is indeed present in the data.

We then investigate the issue of the width of the line. For that purpose, we first compare the *ASCA/RXTE* data to a model with static reflection (i.e., ignoring the relativistic effects) and a narrow Gaussian line. This yields a fit worse by  $\Delta\chi^2 = +9$  compared to the fit in Table 2. This means that indeed the data are much better described by the line and reflection being relativistically smeared than by static line and reflection. Still, the disc inner radius is only weakly constrained by relativistic smearing, to  $r_{\text{in}} \lesssim 50$  (in which fit we assumed the inner radius of the blackbody disc emission constant). Also, the value of the power-law index of reflection emissivity (Section 3.1) is only weakly constrained to  $s \sim 2.1^{+0.5}_{-0.7}$ . In order to compare with results of C98, we also considered a broad Gaussian line in the static-reflection model, obtaining a rather large width of  $\sigma_{\text{Fe}} = 1.18^{+0.26}_{-0.22}$  keV (somewhat more than the values given by C98). Since uncertainties in the *RXTE/PCA* response matrix are not yet fully understood, we have checked our results by ignoring PCA data below 10 keV, in which case the Fe line parameters were constrained by *ASCA* data only. The results for the line energy and width turn out to be very similar to these obtained from the overlapping *ASCA/RXTE* data. Thus, our conclusion is that the Fe  $K\alpha$  line in the soft state of Cyg X-1 is broad.

The reflecting medium is ionized, with  $\xi = 350^{+250}_{-120}$  erg cm s $^{-1}$ . Though observations on May 22–23 (data sets 1–2) and June 17–18 (data sets 4–9) yield higher values of  $\xi$  (see Table 2), those values are relatively weakly constrained and most of the data are consistent with the *ASCA/RXTE* result within 90 per cent confidence. Note that this ionization, obtained with our physical incident continuum, is much weaker than that found with our phenomenological, broken-power law, continuum in Section 3.2, which shows the sensitivity

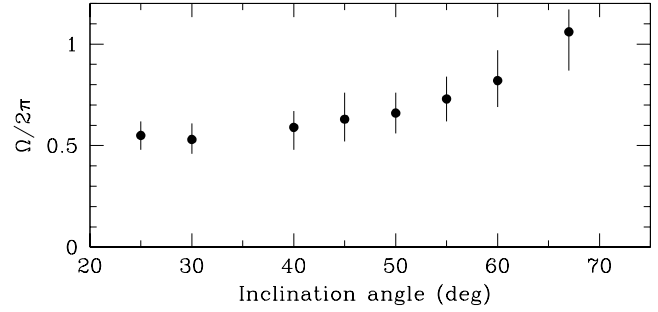


**Figure 10.** The dependence between the solid angle subtended by the reflector,  $\Omega/2\pi$ , and the assumed inclination angle,  $i$ . The error bars are given for 90 per cent confidence.

of the fitted ionization parameter to the shape of the continuum around 7 keV.

The ionization state found here corresponds to a distribution of Fe ions peaking at Fe XXIII $^{+1}_{-n}$ , and with Fe XXIV–XXVI constituting  $\sim 30$  per cent of the ion population. Due to resonant trapping followed by the Auger effect (e.g. Ross & Fabian 1993),  $K\alpha$  photons following ionization of Fe XVII–XXIII ions are completely destroyed and yield no contribution to the observed line. We thus would expect only a line from Fe XXIV–XXVI at  $\sim 6.7$ –7.0 keV. Instead, our model yields the rest-frame centre energy of  $E_{\text{line}} = 6.37 \pm 0.14$  keV for the *ASCA/RXTE* data and  $\sim 6.3$ –6.5 keV for other *RXTE* observations. This inconsistency is likely to be due to our simplified model of reflection, with the ionization state uniform throughout the reflecting medium, whereas the ionization would, in general, vary considerably with the disc radius.

We also consider the Fe abundance,  $A_{\text{Fe}}$ , of the reflector. In all fits so far, we have assumed  $A_{\text{Fe}} = 1$ . We find that indeed  $A_{\text{Fe}} = 1$  is consistent with the data. In particular, the *ASCA/RXTE* data fitted with  $A_{\text{Fe}}$  as a free parameter yield  $A_{\text{Fe}} = 1.0^{+0.6}_{-0.4}$ .

One parameter of Compton reflection which remains relatively uncertain is the inclination angle,  $i$ . As discussed in Section 1, the most conservative range of  $i$  is  $25^\circ \leq i \leq 67^\circ$ . The resulting  $\Omega/2\pi \simeq 0.5$ –1.0, increasing with the increasing  $i$ , is shown in Figure 10. At the Doppler-tomography limit of  $i = 55^\circ$  of Sowers et al. (1998),  $\Omega/2\pi = 0.73 \pm 0.11$ . Our fits favour large inclinations angles:  $\chi^2 = 626, 618, 612$  (for 574 d.o.f.) at  $i = 25^\circ, 45^\circ, 67^\circ$ , respectively, similarly to a recent result of Done & Życki (1999) for the hard state of Cyg X-1. On the other hand, the plasma and disc properties, e.g., the values of  $\ell_h/\ell_s, \ell_{\text{nth}}/\ell_h, \tau_1, T_{\text{max}}$ , are only weakly dependent on  $i$ .

### 3.8 Inclination and the black-hole mass

If we assume the disc extends to the minimum stable orbit in Schwarzschild metric,  $r_{\text{in}} = 6$ , the *ASCA/RXTE* data yield  $M_X = 13.3^{+1.0}_{-0.8} M_\odot$  at the assumed  $D = 2$  kpc,  $f_{\text{col}} = 1.7$  and  $i = 45^\circ$ . We note that this mass range is *above* that allowed by equation (2) at  $i = 45^\circ$ . However, as found in Section 3.7, the model parameters other than  $\Omega/2\pi$  are insensitive to the assumed value of  $i$ . Thus,  $M_X$  can be rescaled to other values of  $i$  using equation (A10), which yields

$$M_X = \frac{11.2_{-0.7}^{+0.8} M_\odot}{\cos^{1/2} i}, \quad (6)$$

which holds for our data to an accuracy better than 2 per cent. This range of  $M_X$  overlaps with that of equation (2) provided,

$$0.13 \lesssim \frac{\sin^3 i}{(1 - \sin^2 i)^{1/4}} \lesssim 0.28, \quad (7)$$

which is satisfied for  $29^\circ \lesssim i \lesssim 39^\circ$ , corresponding [equation (6)] to  $14 \gtrsim M_X/M_\odot \gtrsim 11$ . These are the mass and inclination ranges both consistent with fitting the X-ray data with a disc extending to the minimum stable orbit and satisfying the constraints on the mass function and the mass ratio presented in Section 1.

However, this estimate neglects GR effects in the vicinity of a black hole, namely gravitational redshift and focusing. We can estimate these effects by introducing two factors,  $f_{\text{GR}}$  and  $g_{\text{GR}}$ , correcting the colour temperature and the integrated flux, respectively (Zhang, Cui & Chen 1997a; Cunningham 1975). Then, the correction factor to the mass for a non-rotating black hole,  $r_{\text{in}} = 6$ , and  $i \sim 35^\circ$  to the mass is  $g_{\text{GR}}^{-1/2} f_{\text{GR}}^2 \approx 0.83$  (with a slow dependence on  $i$ ). Thus, the above mass range becomes

$$M_X \approx (10 \pm 1) M_\odot, \quad (8)$$

which represents our best mass estimate including GR corrections. We note that this agrees very well with the estimates of Dotani et al. (1997) and C98 obtained using a GR disc model (after rescaling from  $D = 2.5$  kpc used by them to 2 kpc).

This estimate is sensitive to uncertainties in the distance and the factor  $f_{\text{col}}$ , with  $M_X \propto D f_{\text{col}}^2$ . E.g., a 20 per cent uncertainty in  $D f_{\text{col}}^2$  would increase the range of  $i$  and  $M_X$  (after the GR correction) to  $27^\circ \lesssim i \lesssim 42^\circ$ ,  $14 \gtrsim M_X/M_\odot \gtrsim 7$ .

Above, we assumed  $r_{\text{in}} = 6$ . However, the data do not require that. When we allow  $r_{\text{in}}$  to be a free parameter, the shape of the disc spectrum changes, and we find this change large enough to constrain  $r_{\text{in}}$  by the *ASCA/RXTE* data. Namely, the model fit to the data is improved by  $\Delta\chi^2 = -6$  at  $r_{\text{in}} = 17_{-8}^{+26}$ . Other disc parameters are now  $kT_{\text{max}} = 375_{-5}^{+3}$  eV and (at  $i = 45^\circ$  and before the GR correction)  $M_X = 10_{-7}^{+10} M_\odot$ . In contrast to the  $r_{\text{in}} = 6$  case, no additional constraints on the disc inclination can now be obtained from the X-ray data. However, our PN disc model does not take into account relativistic corrections to the shape of the observed disc-blackbody spectrum. Thus, this result should be treated simply as a demonstration that the inner radius of a blackbody disc can, in principle, be constrained by X-ray spectral fits.

On the other hand, evolution of power spectra, X-ray time lags and the coherence function indicate that on 1996 May 30 (when the *ASCA/RXTE* observation fitted above was performed) the source was still in transition from the hard to the soft state, and the soft state was established only later, in particular during the *RXTE/OSSE* observations of 1996 June 17-18 (Cui et al. 1997). This would then support our finding of  $r_{\text{in}} > 6$  during the *ASCA/RXTE* observation.

### 3.9 Energy balance

If the hot plasma (either homogeneous or patchy) forms a static corona above the disc, energy balance can be used to obtain the fraction of the gravitational energy released in the corona,  $f$  (Svensson & Zdziarski 1994, hereafter SZ94). The general solution to this problem is given by equation (B8) in Appendix B. We assume here isotropic emission of the corona (corresponding to  $d = 1$  in that equation). The reflection albedo,  $a$ , is computed to be  $a \simeq 0.25$  using our *ASCA/RXTE* model spectrum at  $i = 65^\circ$ , at which the strength of Compton reflection is approximately equal to the reflection strength averaged over the  $2\pi$  solid angle (Magdziarz & Zdziarski 1995). Since the plasma is optically thin, we assume the scattering probability,  $p_{\text{sc}} \approx \tau_i \approx 0.25$ . For the *ASCA/RXTE* model spectrum in the case of a homogeneous corona (see Section 3.4), we find the ratio of the hard flux,  $F_h$  (without including reflection) to the soft flux,  $F_s$ , of  $F_h/F_s \approx 0.50$ . (The difference between this ratio and  $\ell_h/\ell_s$  is due to scattering of soft photons in the corona.) This corresponds to  $L_h/L_s = 2(F_h/F_s) \cos i$  (see Appendix B). At  $i = 35^\circ$  (see Section 3.8),  $L_h/L_s \approx 0.82$ . Equation (B8) yields then  $f \approx 0.63$ . Thus, the geometry with a corona covering most of an inner disc is possible in the soft state.

On the other hand, the corona may be patchy (Haardt, Maraschi & Ghisellini 1994; Stern et al. 1995; Poutanen & Svensson 1996). We have investigated that possibility by adding an additional blackbody disc component to our model. The emission of that component corresponds to the fraction of the disc photons that are not passing through the corona. The remaining fraction,  $g'$ , corresponding to the disc photons that are incident on the hot plasma, is  $g' \geq g$  (where  $g$  the covering fraction defined in Section 3.4) because the active regions of the patchy corona can be elevated above the disc surface. We have found that the addition  $g'$  as a free parameter improves the fit by  $\Delta\chi^2 = -9$ , i.e., it is statistically significant. At the best fit, at which  $g' = 0.55$ , the flux ratio is  $F_h/F_s = 0.53$ . This then gives, from equation (B8),  $f = 0.46$ , relatively close to  $f$  in the homogeneous-corona case in the paragraph above.

### 3.10 Luminosity and accretion rate

The total luminosity in the soft state is, using the *ASCA/RXTE* spectrum (see Appendix B),

$$L = L_h + L_r + L_s = 4\pi D^2 \left[ F_h(1 + a\Omega/2\pi) + \frac{F_s}{2 \cos i} \right]. \quad (9)$$

The observed  $F_h = 3.9 \times 10^{-8}$  erg cm $^{-2}$  s $^{-1}$  and  $F_s = 7.8 \times 10^{-8}$  erg cm $^{-2}$  s $^{-1}$  yield, at  $i = 35^\circ$ ,  $L \approx 4.5 \times 10^{37}$  erg s $^{-1}$ . This corresponds to  $\sim 0.03 L_E$  at  $M_X = 10 M_\odot$ . Here,  $L_E \equiv 4\pi\mu_e GM_X c m_p / \sigma_T$  is the Eddington luminosity, where  $\mu_e = 2/(1 + X)$  is the mean electron molecular weight and  $X \approx 0.7$  is the hydrogen mass fraction.

If we assume  $r_{\text{in}} = 6$  and no advection, this corresponds to  $\dot{m} \equiv \dot{M} c^2 / L_E \approx 0.5$ , or  $\dot{M} \approx 8 \times 10^{17}$  g s $^{-1}$ . On the other hand,  $\dot{M}$  can be obtained from fitting the disc model at known  $M_X$  and  $L_s/L$ , see equation (A7). As expected, this yields the same  $\dot{M}$  as above.

## 4 DISCUSSION

#### 4.1 Geometry and scaleheight of the corona

We consider here constraints on the geometry of the X $\gamma$  source from the plasma compactness. For the model spectrum for the *ASCA/RXTE* data,  $L_h \approx 1.9 \times 10^{37}$  erg s $^{-1}$  (see above). The hard compactness is constrained to  $2 \lesssim \ell_h \lesssim 7$ , which follows from  $5 \lesssim \ell_s \lesssim 20$  and  $\ell_h/\ell_s \approx 0.36$  (Section 3.5). From equation (3), we find the characteristic radius of the hot corona is then  $R_h \approx (H/gR_h)(1.2-4) \times 10^7$  cm. At the black-hole mass of  $10M_\odot$  (see Section 3.8), this corresponds to  $R_h \approx (8-30)(H/gR_h)R_g$ .

We can determine  $H$  if we assume hydrostatic equilibrium of the corona. The pressure in the corona has contributions from radiation, thermal and non-thermal electrons and ions, and magnetic field. We find that if the ion temperature,  $T_i$ , equals  $T_e$ , the dominant contribution to pressure in the corona is from radiation. We use then equation (45) in SZ94 to estimate  $H/R_h \sim 10^{-2}$  in the case of a homogeneous corona ( $g = 1$ ) at the radius of maximum disc dissipation per log  $R$ ,  $17R_g$ . This would imply a rather small size of the plasma,  $R_h \lesssim 0.3g^{-1}R_g$ , violating our assumption of a homogeneous corona, and thus implying  $g \ll 1$ . On the other hand,  $T_i \gg T_e$  is a likely condition in many astrophysical situations, e.g., two-temperature coronae are considered by Di Matteo, Blackman & Fabian (1997). In addition, ions can be accelerated to non-thermal energies, in addition to accelerated electrons. Then, the corona may be supported by the ion pressure, together with the pressure of an equipartition magnetic field.

We can constrain the average energy of ions by requiring that the rate of Coulomb energy transfer from the ions (both thermal and non-thermal) to electrons corresponds a luminosity,  $L_{\text{Coulomb}}^{\text{ie}} \ll L_h$ , which follows from our fits, in which  $\ell_{\text{th}} \ll \ell_h$ . This, via the condition of hydrostatic equilibrium, constrains in turn the scaleheight of the corona. We then obtain, using equations (1) and (3) in Zdziarski (1998),

$$\frac{H}{R_h} \approx 2 \times 10^2 \Theta_e^{3/2} \tau_{\text{th}}^{-2} \frac{L_{\text{Coulomb}}^{\text{ie}}}{L_E} \approx \frac{L_{\text{Coulomb}}^{\text{ie}}}{L_h}, \quad (10)$$

where  $\Theta_e \equiv kT_e/m_e c^2$ , and which holds independent of radius. In the second equality, we used the numerical values of the parameters corresponding to the plasma in Cyg X-1. Then, e.g.,  $H/R_h = 0.3$  (corresponding to  $\ell_{\text{th}}/\ell_h \sim 0.3$ , see Section 3.5) would correspond to  $R_h \approx (6-20)R_g$  at the covering fraction of  $g \approx 0.5$  (Section 3.9). Thus, the hot plasma can extend over a substantial part of the disc region where most of the gravitational energy is dissipated. We note that  $H/R_h$  of equation (10) corresponds sub-virial ions,  $kT_i/m_p c^2 \sim 0.05/r$ .

On the other hand, the corona is not necessarily in the hydrostatic equilibrium (e.g. Beloborodov 1999). Some of the power released in the corona can be used to accelerate it to some velocity,  $\beta c$ . We can constrain  $\beta$  by considering the power (or kinetic luminosity),  $L_{\text{kin}}$ , of the outflowing ions, which equals to the number flux times the bulk-motion energy times area. This yields

$$\frac{L_{\text{kin}}}{L_h} \approx \frac{m_p}{m_e} \frac{\tau \beta^3}{2\ell_h}. \quad (11)$$

For  $\tau \sim 0.25$  and  $2 \lesssim \ell_h \lesssim 7$  (Section 3.5),  $\beta \gtrsim 0.3(L_{\text{kin}}/L_h)^{1/3}$ . Since no apparent effects of eventual dissipation of  $L_{\text{kin}}$  are observed from Cyg X-1, probably  $L_{\text{kin}} \ll$

$L_h$ . Then, equation (11) allows for a mildly relativistic outflow, e.g.,  $\beta \sim 0.2$  at  $L_{\text{kin}} \approx 0.2L_h$  and  $\ell_h = 7$ .

#### 4.2 Coulomb interactions and plasma heating

As found in Section 3.5, the *ASCA/RXTE* data require  $7 \lesssim \ell \lesssim 27$ . The upper limit is due to effects  $e^+e^-$  pair production and annihilation, and the lower limit is due to energy loss of non-thermal electrons by Coulomb scattering.

The origin of the lower limit has been discussed by Poutanen (1998, see also Zdziarski et al. 1990). For completeness, we discuss it in some detail here. The energy loss rate due to Compton scattering is (e.g. Rybicki & Lightman 1979)

$$\dot{\gamma}_{\text{Compton}} \approx -\frac{4}{3} \frac{\sigma_T}{m_e c} (\gamma^2 - 1) U_{\text{ph}}, \quad (12)$$

where  $U_{\text{ph}}$  is the energy density of photons for which Compton scattering is in the Thomson limit. For a homogeneous, optically-thin, spherical source of radius  $\mathcal{R}$  and with luminosity  $\mathcal{L}$ , the energy density is roughly

$$U_{\text{ph}} \approx \frac{\mathcal{L}}{(4/3)\pi \mathcal{R}^3} \frac{\mathcal{R}}{c} = \frac{3}{4\pi} \frac{m_e c^2}{\sigma_T} \frac{\ell}{\mathcal{R}}, \quad (13)$$

where we use  $\ell \approx \ell_s + \ell_h$  for the soft state of Cyg X-1, in which most of photons in the observed spectrum are in the Thomson limit. On the other hand, the Coulomb energy loss rate due to interaction of an electron of  $\gamma \gg 1$  and  $\gamma - 1 \gg \Theta_e$  with a background thermal plasma is given by (Gould 1975; Frankel, Hines & Dewar 1979; Coppi & Blandford 1992)

$$\dot{\gamma}_{\text{Coulomb}} \approx -\frac{3}{2} \frac{c}{\mathcal{R}} \tau_{\text{th}} \ln(\Lambda \gamma^{1/2}) \quad (14)$$

where  $\Lambda = [2\mathcal{R}/(3a_0\tau_{\text{th}})]^{1/2}$  and  $a_0 = 5.29 \times 10^{-9}$  cm is the Bohr radius. Then, two rates are equal at a critical Lorentz factor given by

$$\gamma_{\text{cr}}^2 \approx \frac{3\pi\tau_{\text{th}}}{2\ell} \ln \Lambda + 1. \quad (15)$$

Note that  $\gamma_{\text{cr}}$  depends on  $\mathcal{R}$  only weakly via  $\ln \Lambda$ , and thus this results is nearly-independent of the source geometry. Since  $\dot{\gamma}_{\text{Coulomb}} \propto \gamma^0$  while  $\dot{\gamma}_{\text{Compton}} \propto \gamma^2$ , the Coulomb energy loss is so fast that it creates a break at  $\gamma_{\text{cr}}$  in the non-thermal distribution. This then results in a break in the distribution of scattered photons, which is *not* seen in our data. Also, the energy lost by the non-thermal electrons strongly heats the thermal plasma, increasing its temperature. These effects are especially pronounced for  $\Gamma_{\text{inj}} > 2$  (as is the case in our models), when most of the non-thermal energy is provided to accelerated electrons at the low-energy end of their distribution.

Since  $\gamma_{\text{crit}} \propto \ell^{-1/2}$ , the observed lack of signatures of the above effect constrains  $\ell$  from below. At the lower limit of  $\ell \approx 7$ , and at  $\tau_{\text{th}} = 0.25$ ,  $\mathcal{R} = 10^8$  cm,  $\gamma_{\text{cr}} \approx 2$ , i.e., Coulomb interactions just begin to affect the low-energy end of the non-thermal distribution. Figure 7 illustrates the effect of varying compactness on the spectral shape.

In most our fitted models, we found Coulomb heating of the thermal plasma sufficient to maintain the plasma temperature required by the observed spectral shape,  $kT_e \sim 50$  keV (which, we note, is much higher than the Compton temperature,  $\sim 1$  keV, at which the net energy transfer via

Compton scattering between electrons and photons of the observed spectrum would be null). Thus,  $\ell_{\text{nth}}/\ell_{\text{h}} \approx 1$  in those models (Section 3.5). However, this result depends on  $\gamma_{\text{min}}$ , which has been set so far to 1.3. A higher value of  $\gamma_{\text{min}}$  would decrease the Coulomb heating and would require some additional heating of the thermal plasma component. For example, the *ASCA/RXTE* data fitted with  $\gamma_{\text{min}} = 3$  gives  $\ell_{\text{nth}}/\ell_{\text{h}} = 0.62$ , i.e., additional heating is required. However, that this fit is worse by  $\Delta\chi^2 \approx +9$  with respect to the fit with  $\gamma_{\text{min}} = 1.3$ . Thus,  $\gamma_{\text{min}}$  is constrained by the data to be  $\sim 1$ .

Some additional heating of the thermal electrons can be due to the Coulomb energy transfer from energetic ions, see Section 4.1. The ions can be thermal or non-thermal. Acceleration of ions is, in fact, quite likely, and not in conflict with the data. In Section 3.5, we found that the electron acceleration rate,  $\dot{N}_{\text{inj}}$ , is soft, with most of the accelerated electrons near  $\gamma_{\text{min}} \sim 1$ . If acceleration of ions follows a similar law, most of accelerated ions will have energies close to the low-energy end of the power law, and effects of pion and pair production by ions will be negligible. On the other hand, the accelerated ions will provide some contribution to Coulomb heating of the thermal electrons (and to the pressure in the plasma), which contribution is allowed by the data as long as the average ion energy is  $\lesssim 50\text{MeV}/r$  (see Section 4.1). We also note that the energetic ions would transfer some energy to the non-thermal electrons via Coulomb scattering. However, this rate, inversely proportional to the ion mass, is found by us to be negligible compared to the energy loss rate of non-thermal electrons to the thermal ones [equation (14)].

Another mechanism of heating the thermal electrons is the so-called synchrotron boiler (Ghisellini, Guilbert & Svensson 1988; Ghisellini, Haardt & Svensson 1998; Svensson 1999). In this process, thermal electrons are heated by synchrotron reabsorption of photons emitted by the non-thermal electrons.

### 4.3 Anisotropy effects

As stated in Section 3.4, our Comptonization model assumes all the distributions (photons and  $e^\pm$ ) to be homogeneous and isotropic. This approximation may not hold in some geometries. In particular, in the disc-corona geometry, the seed photons enter the corona from below only. Thus, their distribution is anisotropic. Then, a soft photon emitted by the disc surface is much more likely to scatter on an energetic electron moving down rather than up. This is because the scattering probability is  $\propto 1 - (v/c) \cos \vartheta$ , where  $v$  is the electron speed and  $\vartheta$  is the angle between the directions of the electron and the photon. This anisotropy affects in different ways spectra from non-thermal and thermal plasmas (and their  $e^\pm$  distributions), and thus we discuss them separately.

The case of a relativistic, non-thermal  $e^\pm$  distribution is studied by Ghisellini et al. (1991). Their results show that the angle-averaged downward flux, due to a single Compton scattering by isotropic electrons with  $\gamma \gg 1$ , is  $\sim 3$  times larger than the flux emitted upwards at the angle of  $45^\circ$ . This would result in a corresponding strong enhancement of the Compton-reflected component, which effect is clearly not seen in our data. This enhancement could be much smaller

if the hot plasma forms an inner hot disc and emission of seed photons and reflection are from an outer optically-thick disc.

On the other hand, the steady-state non-thermal electron distribution in a disc corona is unlikely to be isotropic. This is because electrons directed downward lose energy much faster than those directed upward, due to precisely the same effect as that discussed above. The main mechanism for their isotropisation is Coulomb interaction since higher-order Compton scatterings are negligible in our case with  $\tau_{\text{nth}} \sim 10^{-2}$ . The process of Coulomb interactions of non-thermal electrons with the background thermal plasma is considered in Section 4.2 above, where we find that the observed spectrum constrains compactness to a range where the electron energy losses due to this process are negligible compared to those due to Compton scattering. Then the negligible energy losses, in the case of  $e^\pm e^\pm$  scattering, imply no significant changes of the direction of the relativistic electrons. (The rate of interactions of relativistic electrons with protons, which could change the electron direction without significant energy loss, is smaller than that with  $e^\pm$  by a factor  $m_e/m_p$  and thus even less significant.) Thus, the steady-state distribution of electrons with  $\gamma > \gamma_{\text{cr}} [\gtrsim 2$ , equation (15)] will be strongly anisotropic due to the Compton energy loss rate depending on the direction.

When this is the case, an isotropic acceleration/injection of relativistic electron will lead to *isotropic* emission of singly-scattered photons. This is because the effects of anisotropic emission and anisotropic energy loss cancel each other, and the rate of emission in a given direction is simply proportional to the injection rate (see Ghisellini et al. 1991).

Note that an anisotropic electron distribution corresponds to a current in the plasma. This current will be balanced by an opposite current in the thermal component of the electron distribution. Since  $\tau_{\text{th}} \gg \tau_{\text{nth}}$ , the latter current will have a negligible effect on the properties of the thermal plasma component.

Anisotropy effects in the case of a thermal  $e^\pm$  distribution are considered by Haardt (1993), Stern et al. (1995) and Poutanen & Svensson (1996). They are due to the same physical effect as described above, and thus they suppress a part of the emitted spectrum due to the first (and to some degree, second) order of Compton scattering. On the other hand, photons become closely isotropic after a higher number of scatterings. This leads to the so-called anisotropy break close to the peak energy of the second-order scattering. In contrast to the non-thermal case, we have found that the Coulomb relaxation time for the thermal electrons interacting with themselves is about equal to the thermal plasma cooling time ( $\sim 10^{-4}$  s), and thus no significant anisotropy of the thermal electron distribution is expected in our case.

In order to assess the significance of the thermal anisotropy break in the case of Cyg X-1, we have performed Monte-Carlo simulations for a slab geometry assuming the plasma parameters as found from data fitting. We have found the anisotropy break at  $\sim 15$  keV, with the outward flux at 7 keV suppressed by a factor of  $\sim 0.8$  with respect to the isotropic case. As seen in Figure 9 (the dashed curve), this break energy actually coincides with the break occurring due to intersections of the power laws due to thermal and non-thermal scattering. Then, plasma parameters slightly

different from those determined neglecting anisotropy effects could still produce the observed spectrum. Thus, the present data are still consistent with the presence of a thermal anisotropy break.

On the other hand, if the mildly relativistic outflow is present in the corona (see Section 4.1), the seed soft radiation emitted by the disc is more isotropic in the rest frame of the outflowing plasma, thus reducing the amplitude of the anisotropy break (see Beloborodov 1998, 1999).

#### 4.4 Disc stability

We examine here the stability of the optically-thick disc, taking into account the fraction,  $f$ , of the gravitational energy being dissipated in the corona (SZ94). A possible mechanism for energy transfer from the disc to the corona are magnetic flares (e.g. Galeev, Rosner & Vaiana 1979; Beloborodov 1999). A part of the disc becomes radiation-pressure dominated and thus unstable (both thermally and viscously) above a critical accretion rate,  $\dot{m}_{\text{cr}}$ . We find that a radiation-pressure dominated zone in a PN disc appears first (with increasing  $\dot{m}$ ) around  $R = 15.1R_{\text{g}}$ . We then extend results of SZ94 (who considered the Newtonian potential) to the case of the PN potential, and derive  $\dot{m}_{\text{cr}}$  in the presence of external dissipation as,

$$\dot{m}_{\text{cr}} = 0.64(\alpha M_{\text{X}}/M_{\odot})^{-1/8}[(1-f)\zeta]^{-9/8}, \quad (16)$$

where  $\alpha$  is the viscosity parameter and  $\zeta$  is a parameter in the vertically-averaged radiative transfer equation, which is set by various authors between 0.5 and 2. We follow here Shakura & Sunyaev (1973) and set  $\zeta = 1$  (which value is in approximate agreement with calculations taking into account the vertical disc structure, A. Rózańska, private communication). We note that relativistic effects, as approximated by the PN potential, have a stabilizing effect on the disc, i.e., they increase the value of  $\dot{m}_{\text{cr}}$ . Specifically, the numerical coefficient in equation (16) is only 0.37 in the Newtonian case (SZ94).

At  $M_{\text{X}} = 10M_{\odot}$ ,  $f = 0.63$ ,  $\dot{m}_{\text{cr}} \approx 1.47\alpha^{-1/8}$ . This implies that the disc in the soft state of Cyg X-1, with  $\dot{m} \approx 0.5$  (Section 3.10), is stable at any  $\alpha$ . Figure 11 shows the solutions of the optically thick accretion disc with the corona for 4 values of  $f$ .

On the other hand, the data do not require  $r_{\text{in}} = 6$ , and a fit in Section 3.8 gives  $r_{\text{in}} = 17_{-8}^{+26}$ . This solution corresponds to a higher  $\dot{m}$  and a lower  $M_{\text{X}}$  than in the case of  $r_{\text{in}} = 6$ . Then,  $\dot{m}$  may possibly exceed  $\dot{m}_{\text{cr}}$  and the disc instability may be responsible for the large  $r_{\text{in}}$ . The precise value of  $\dot{m}$  in this case depends on the unknown partition of the observed luminosity into the fractions from the corona above the disc and an inner hot flow at  $r < r_{\text{in}}$ , possibly advective (Narayan & Yi 1995; Abramowicz et al. 1995). Therefore, the current data do not allow us to distinguish between the possibilities of  $r_{\text{in}} = 6$  and  $> 6$ .

#### 4.5 Alternative models

One alternative model to the non-thermal Compton model presented here is thermal Comptonization, which was proposed to model spectra of the soft state of Cyg X-1 (Poutanen et al. 1997; C98; Esin et al. 1998) and other black-hole

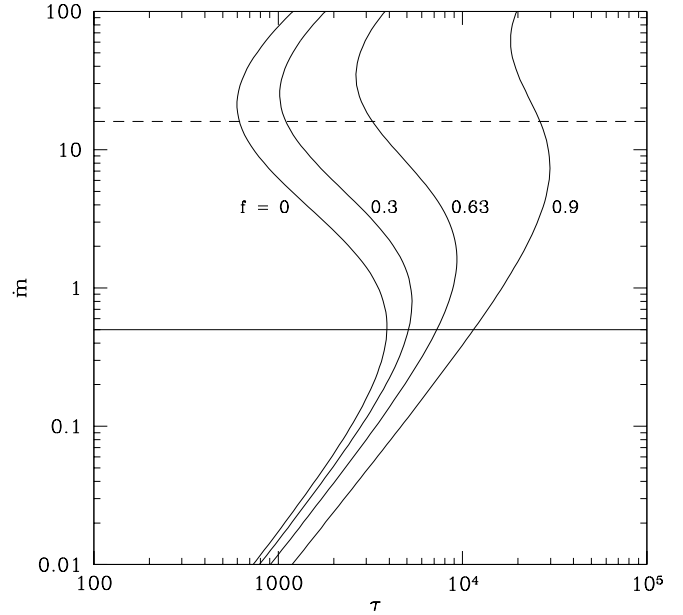


**Figure 11.** The solutions of the optically thick disc (Abramowicz et al. 1988) with a fraction of accretion power,  $f$ , dissipated in the corona (SZ94), for  $M_{\text{X}} = 10M_{\odot}$  and  $\alpha = 0.1$  at the radius of the most significant instability of  $R = 15.1R_{\text{g}}$ . The curves are labeled by their value of  $f$ , with  $f = 0.63$  corresponding for Cyg X-1. The solid and dashed horizontal lines correspond to the accretion rate of Cyg X-1 in the soft state and to the Eddington luminosity at an efficiency of  $\eta = 1/16$ , respectively.

binaries (Miyamoto et al. 1991; Esin et al. 1997) However, as discussed in Section 3.3, this process is unable to account for the observed steep power-law tails extending to high energies.

Another possibility for the production of the power-law spectra observed in the soft state is that of bulk-motion Comptonization (see, e.g., Payne & Blandford 1981; Colpi 1988; Laurent & Titarchuk 1999). If there is quasi-spherical accretion near the black hole, then cold infalling electrons could acquire substantial velocities  $v \sim c$ , and Comptonization using the large bulk inflow velocity of the electrons (as opposed to their assumed smaller thermal motions) could give rise to power law spectra like those observed in the soft state. This model predicts a sharp cutoff in the spectrum at a few hundred keV. The OSSE data, on the other hand, clearly show no cutoff until at least 800 keV which strongly rules out the bulk Comptonization hypothesis.

Also, only a fraction,  $\ll 1$ , of the disc blackbody photons (emitted semi-isotropically with maximum emission per  $\log r$  at  $r \sim 20$ ) will be incident on the inner spherical inflow (see Figures 1–2 in Laurent & Titarchuk 1999). This appears to lead to a normalization of the tail spectrum with respect to the disc blackbody much below the observed normalization. Furthermore, the presence of the Compton reflection with a covering factor of  $\Omega/2\pi \sim 0.7$  puts strong constraints on the geometry of the accretion flow. Such a covering factor is natural in a disc-corona geometry, but it appears incompatible with the bulk Comptonization scenario (Figures 1–2 in Laurent & Titarchuk 1999).

#### 4.6 The nature of state transition

A remarkable feature of state transitions in Cyg X-1 is that the associated change in the bolometric luminosity is very small. We have found  $L \approx 4.5 \times 10^{37}$  erg s<sup>-1</sup> in the soft state (Section 3.10), whereas the maximum bolometric luminosity observed in the hard state is  $\sim 3 \times 10^{37}$  erg s<sup>-1</sup> (G97; at  $D = 2$  kpc). If there is no advection, the corresponding change of  $\dot{M}$  is small. In the simplest scenario, we expect no advection in the soft state provided the optically-thick disc extends to the minimum stable orbit. On the other hand, a commonly used model for the hard state comprises a hot inner disc (Poutanen, Krolik & Ryde 1997; Poutanen & Coppi 1998; Poutanen 1998; Esin et al. 1998), in which case advection is likely. If the transition from the hard state to the soft one is associated with an increase of  $\dot{M}$ , both that increase and the advected fraction of the power in the hard state have to be very small (Esin et al. 1998). On the other hand, advection may dominate over cooling in the hard state, in which case the hard-to-soft transition would be associated with a *decrease* of  $\dot{M}$ .

In either of the above cases, the hard-to-soft state transition appears to be associated with a decrease of the minimum radius of the optically-thick disc,  $R_{\text{in}}$ . When  $R_{\text{in}}$  is large, the inner disc is hot and it receives a major fraction ( $\sim 0.9$ ) of the available gravitational energy. The spectrum is hard,  $\Gamma \sim 1.6$ , and the covering angle of the reflector is relatively small,  $\Omega/2\pi \sim 0.3$ . At a certain moment, the cold disc starts to move inwards, taking in more and more accretion power, while the hot phase diminishes. In the final configuration the cold disc extends down to near the last stable orbit, while the hot (non-thermal) plasma probably forms a corona above that disc, receiving less of accretion power ( $\sim 0.6$ ) than in the hard state. This results in a softening of the spectrum, to  $\Gamma \sim 2.5$ , and an increase of the strength of the Compton-reflection component, to  $\Omega/2\pi \sim 0.7$ .

Another possible model for the hard state has recently been proposed by Beloborodov (1999). In that model, the X $\gamma$  source forms a corona above optically-thick disc extending close to the minimum stable orbit even in the hard state. The hardness of the spectrum and the weakness of Compton reflection in that state are then explained by a mildly-relativistic bulk motion away from the disc. The hard-to-soft state transition would then involve the corona becoming static. Possibly, this may be due to the coronal plasma consisting of  $e^+e^-$  pairs in the hard state (which is allowed by the form of hard-state spectrum, G97; Poutanen & Coppi 1998), and of an ordinary plasma in the soft state. The data studied here appear not to allow distinguishing between these possibilities.

## 5 CONCLUSIONS

In this work, we have obtained a self-consistent description of the soft state of Cyg X-1 (observed in 1996 by *ASCA*, *RXTE* and *OSSE*) in terms of a (predominantly) non-thermal corona above the surface of an optically-thick accretion disc. Emission of the non-thermal corona accounts for both the high-energy power-law tail observed up to several hundred keV and the soft excess, resolving two problems of the thermal-plasma model of C98.

The non-thermal corona receives most of the supplied power in the form of electrons accelerated (or injected) to relativistic energies. The acceleration rate is rather soft, with the power-law index of  $\Gamma_{\text{inj}} \sim 2.5\text{--}3$  above  $\gamma_{\text{min}} \sim 1$ . The electrons lose their initial energy in Compton and Coulomb processes, and finally form a thermal component (at  $kT_e \sim 50$  keV) of their distribution at low energies. The resulting X $\gamma$  spectrum consists of blackbody photons emitted by the disc (at low energies) and a component due to Compton upscattering of the disc photons by both thermal and non-thermal electrons in the corona.

Production of  $e^+e^-$  pairs is negligible in the corona, which follows from the observed lack of an annihilation feature in the spectrum from *OSSE*. This constrains from above the compactness (a ratio of the luminosity to the size),  $\ell$ , of the source. On the other hand, Coulomb scattering is an important process in heating the thermal electrons by the non-thermal ones. Still, the Coulomb energy loss by non-thermal electrons is constrained by the observed spectrum to be slower than their Compton energy loss, which constrains  $\ell$  from below. The resulting constraints are  $7 \lesssim \ell \lesssim 30$ .

We also find that a modest heating of the thermal electrons (in addition to their Coulomb heating by the non-thermal electrons) is required by the observed spectrum. This heating can be provided by Coulomb interactions with energetic ions in the corona, which then also provide most of the pressure support of the corona.

The coronal geometry of the source is supported by the observed spectral component from Compton reflection from the disc surface and the Fe broad  $K\alpha$  fluorescence line. Both components are relativistically smeared, supporting reflection from an inner part of the disc. The strength of the observed Compton reflection spectrum is fully consistent with reflection from a slab, after taking into account Compton scattering of reflected photons in the coronal plasma. The observed softness of the spectrum is consistent with energy balance in the disc-corona system with  $f \sim 0.6$  of the available gravitational energy dissipated in the corona (and the remainder within the disc). From the observed luminosity and fitted compactness, we find the corona covers a substantial fraction of the disc provided most of its pressure support is provided from energetic ions. Still, the ion energy in random velocities is constrained to be much below the virial energy (by the constraint on the Coulomb heating of thermal electrons, see above). Then, the corona can be static. On the other hand, we find that a mildly relativistic outflow is also consistent with the observations.

Fits of our PN disc model together with the mass function and constraints on the mass ratio imply  $M_X \simeq (10 \pm 1)M_\odot$  and the inclination of  $i \sim 30^\circ\text{--}40^\circ$ , at the most likely distance of 2 kpc and the colour correction of  $f_{\text{col}} = 1.7$ . The bolometric luminosity is  $\simeq 4.5 \times 10^{37}$  erg s<sup>-1</sup>  $\simeq 0.03L_E$ , which corresponds, in the absence of advection, to  $\dot{m} \simeq 0.5$ . At that accretion rate, the disc is fully stable all the way down to the minimum stable orbit against the instabilities associated with the dominance of radiation pressure. On the other hand, solutions with advection, a higher  $\dot{m}$  and the disc terminating at  $r_{\text{in}} \gg 6$  are also allowed by the data.



**ACKNOWLEDGEMENTS**

The authors are grateful to Chris Done, the referee, for valuable remarks, to Keith Jahoda for help with the PCA data reduction, to Joanna Mikołajewska for discussions on the distance and binary parameters of Cyg X-1, and to Bożena Czerny for providing us with her optically-thick disc code. This research has been supported in part by the Polish KBN grants 2P03D00713, 2P03D00614, 2P03C00511p0(1,4), 2P03D00514, NASA grants and contracts, the Swedish Natural Science Research Council and the Anna-Greta and Holger Crafoord Fund, and it has made use of data obtained through the HEASARC online service provided by NASA/GSFC.

**REFERENCES**

- Abramowicz M. A., Czerny B., Lasota J.-P., Szuszkiewicz E., 1988, *ApJ*, 332, 646
- Abramowicz M. A., Chen X., Kato S., Lasota J.-P., Regev O., 1995, *ApJ*, 438, L37
- Anders E., Ebihara M., 1982, *Geochim. Cosmochim. Acta*, 46, 2363
- Arnaud K. A., 1996, in Jacoby G. H., Barnes J., eds., *Astronomical Data Analysis Software and Systems V*. ASP Conf. Series Vol. 101, San Francisco, p. 17
- Balućńska-Church M., Belloni T., Church M. J., Hasinger G., 1995, *A&A*, 302, L5
- Beloborodov A. M., 1998, *ApJ* 496, L105
- Beloborodov A. M., 1999, *ApJ*, 510, L123
- Björnsson G., Svensson R. 1991, *ApJ*, 371, L69
- Bolton C. T., 1972, *Nat*, 235, 271
- Bowyer S., Byram E. T., Chubb T. A., Friedman M., 1965, *Sci*, 147, 394
- Bregman J., Butler D., Kemper E., Koski A., Kraft R. P., Stone R. P. S., 1973, *ApJ*, 185, L117
- Colpi M., 1988, *ApJ*, 326, 223
- Coppi P. S., 1992, *MNRAS*, 258, 657
- Coppi P. S., 1999, in Poutanen J., Svensson R., eds., *ASP Conf. Ser. Vol. 161, High Energy Processes in Accreting Black Holes*. Astron. Soc. Pac., San Francisco, p. 375
- Coppi P. S., Blandford R. D., 1992, *MNRAS*, 245, 453
- Cui W., Zhang S. N., Focke W., Swank, J. H., 1997, *ApJ*, 484, 383
- Cui W., Ebisawa K., Dotani T., Kubota A., 1998, *ApJ*, 493, L75 (C98)
- Cunningham C. T., 1975, *ApJ*, 202, 788
- Davis R., Hartmann L., 1983, *ApJ*, 270, 671
- Di Matteo T., Blackman E. G., Fabian A. C., 1997, *MNRAS*, 291, L23
- Dolan J. F., Tapia S., 1989, *ApJ*, 344, 830
- Dolan J. F., Crannell C. J., Dennis B. R., Frost K. J., Orwig L. E., 1977, *Nat*, 267, 813
- Done C., Życki P. T., 1999, *MNRAS*, 305, 457
- Done C., Mulchaey J. S., Mushotzky R. F., Arnaud K. A., 1992, *ApJ*, 395, 275
- Dotani T. et al., 1997, *ApJ*, 485, L87
- Ebisawa K., Ueda Y., Inoue H., Tanaka Y., White N. E., 1996, *ApJ*, 467, 419
- Esin A. A., McClintock J. E., Narayan R., 1997, *ApJ*, 489, 865
- Esin A. A., Narayan R., Cui W., Grove J. E., Zhang S. N., 1998, *ApJ*, 505, 854
- Fabian A. C., Rees M. J., Stella L., White N. E., 1989, *MNRAS*, 238, 729
- Frankel N. E., Hines K. C., Dewar R. L., 1979, *Phys. Rev. A*, 20, 2120
- Galeev A. A., Rosner R., Vaiana G. S., 1979, *ApJ*, 229, 318
- Ghisellini G., Guilbert P. W., Svensson R., 1988, *ApJ*, 334, L5
- Ghisellini, G., George, I. M., Fabian, A. C., Done C. 1991, *MNRAS*, 248, 14
- Ghisellini G., Haardt F., Svensson R., 1998, *MNRAS*, 297, 348
- Gierliński M., Zdziarski A. A., Done C., Johnson W. N., Ebisawa K., Ueda Y., Haardt F., Philips B. F., 1997a, *MNRAS*, 288, 958 (G97)
- Gierliński M., Zdziarski A. A., Dotani T., Ebisawa K., Jahoda K., Johnson W. N., 1997b, in Dermer Ch. D., Strickman M. S., Kurfess J. D., eds., *The 4th Compton Symposium*. AIP, New York, p. 844
- Gies D. R., Bolton C. T., 1982, *ApJ*, 260, 240
- Gies D. R., Bolton C. T., 1986, *ApJ*, 304, 371
- Gould R. J., 1975, *ApJ*, 196, 689
- Haardt F., 1993, *ApJ*, 413, 680
- Haardt F., Maraschi L., Ghisellini G., 1994, *ApJ*, 432, L95
- Hanawa T., 1989, *ApJ*, 341, 948
- Herrero A., Kudritzki R. P., Gabler R., Vilchez J. M., Gabler A., 1995, *A&A*, 297, 556
- Holman G. D., Benka S. G., 1992, *ApJ*, 400, L79
- Kaastra J. S., Mewe R., 1993, *A&AS*, 97, 443
- Kato S., Fukue J., Mineshige S., 1998, *Black-Hole Accretion Disks*. Kyoto University Press, Kyoto
- Lampton M., Margon B., Bowyer S., 1976, *ApJ*, 208, 177
- Laurent P., Titarchuk L., 1999, *ApJ*, 511, 289
- Liang E. P., Nolan P. L., 1984, *Space Sci. Rev.*, 38, 353
- Ling J. C. et al., 1997, *ApJ*, 484, 375
- McConnell M. et al., 1996, *ApJ*, 424, 933
- Magdziarz P., Zdziarski A. A., 1995, *MNRAS*, 273, 837
- Malysheva L. K., 1997, *Astron. Lett.*, 23, 585 [in Russian: *AZh Pisma*, 23, 667]
- Margon B., Bowyer S., Stone R. P. S., 1973, *ApJ*, 185, L113
- Massey P., Johnson K. E., DeGioia-Eastwood K., 1995, *ApJ*, 454, 171
- Mises R., 1964, *Mathematical Theory of Probability and Statistics*. Academic Press, New York
- Miyamoto S., Kimura K., Kitamoto S., Dotani T., Ebisawa K., 1991, *ApJ*, 383, 784
- Mitsuda K. et al., 1984, *PASJ*, 36, 741
- Morrison R., McCammon D., 1983, *ApJ*, 270, 119
- Narayan R., Yi I., 1995, *ApJ*, 452, 710
- Ninkov Z., Walker G. A. H., Yang S., 1987, *ApJ*, 321, 425
- Ogawara Y., Mitsuda K., Masai K., Vallerga J. V., Cominsky L. R., Grunsfeld J. M., Kruper J. S., Ricker G. R., 1982, *Nat*, 295, 675
- Paciesas W. S., Robinson C. R., McCollough M. L., Zhang S. N., Harmon B. A., Wilson C. A., 1997, in Dermer Ch. D., Strickman M. S., Kurfess J. D., eds., *The 4th Compton Symposium*. AIP, New York, p. 834
- Paczyński B., Wiita P. K., 1980, *A&A*, 88, 23
- Payne D. G., Blandford R. D., 1981, *MNRAS*, 196, 781
- Philips B. F. et al., 1996, *ApJ*, 465, 907
- Poutanen J., 1999, in Abramowicz M., Björnsson G., Pringle J., eds., *Theory of Black Hole Accretion Disks*, Cambridge University Press, Cambridge, p. 100
- Poutanen J., Coppi P. S., 1998, *Physica Scripta*, T77, 57
- Poutanen J., Svensson R., 1996, *ApJ*, 470, 249
- Poutanen J., Krolik J. H., Ryde F., 1997, *ApJ*, 292, L21
- Press W. H., Teukolsky S. A., Vetterling W. T., Flannery B. P., 1992, *Numerical Recipes*. Cambridge Univ. Press, Cambridge
- Reilman R. F., Manson S. T., 1979, *ApJS*, 40, 815
- Ross R. R., Fabian A. C., 1993, *MNRAS*, 261, 74
- Rybicki G. B., Lightman A. P., 1979, *Radiative Processes in Astrophysics*. Wiley-Interscience, New York
- Shakura N. I., Sunyaev R. A., 1973, *A&A*, 24, 337
- Shimura T., Takahara F., 1995, *ApJ*, 445, 780

Sowers J. W., Gies D. R., Bagnuolo W. G., Shafter A. W., Wiemker R., Wiggs M. S., 1998, *ApJ*, 505, 424  
 Stern B. E., Poutanen J., Svensson R., Sikora M., Begelman M. C., 1995, *ApJ*, 449, L13  
 Svensson R., 1999, in Poutanen J., Svensson R., eds., *ASP Conf. Ser. Vol. 161, High Energy Processes in Accreting Black Holes*. Astron. Soc. Pac., San Francisco, p. 361  
 Svensson R., Zdziarski A. A., 1994, *ApJ*, 436, 599 (SZ94)  
 Walborn N. R., 1973, *ApJ*, 179, L123  
 Webster B.L., Murdin P., 1972, *Nature*, 235, 37  
 Zdziarski A. A., 1998, *MNRAS*, 296, L51  
 Zdziarski A. A., Coppi P. S., Lamb D. Q., 1990, *ApJ*, 357, 149  
 Zdziarski A. A., Lightman A. P., Maciołek-Niedźwiecki A., 1993, *ApJ*, 414, L93  
 Zhang S. N., Cui W., Chen W., 1997a, *ApJ*, 482, L155  
 Zhang S. N., Cui W., Harmon B. A., Paciesas W. S., 1997b, in Dermer Ch. D., Strickman M. S., Kurfess J. D., eds., *The 4th Compton Symposium*. AIP, New York, p. 839  
 Zhang S. N., Cui W., Harmon B. A., Paciesas W. S., Remillard R. E., van Paradijs J., 1997c, *ApJ*, 477, L95

## APPENDIX A: SPECTRUM FROM A PSEUDO-NEWTONIAN DISC WITH ZERO-STRESS INNER BOUNDARY

Let us consider a geometrically-thin, optically-thick, accretion disc around a Schwarzschild black hole with a mass,  $M$ . We assume the disc locally emits a blackbody spectrum, which fraction,  $p_{sc}$  is then partly scattered in a corona. The unscattered flux observed from the disc is given by

$$F_\nu = (1 - p_{sc}) \frac{2\pi \cos i}{f_{col}^4 D^2} \int_{R_{in}}^{\infty} B_\nu(T) R dR, \quad (A1)$$

where  $B_\nu$  is the blackbody spectrum. Other symbols used in this Appendix are defined in Sections 1 and 3.1 except that we now drop subscripts in symbols for the colour temperature and mass. We allow here for truncation of the disc at  $R_{in} \geq R_{ms} = 6GM/c^2$ .

In order to compute the observed spectrum, we need to find the radial colour temperature distribution,  $T(R)$ . The rate of energy generation per unit area of one side of the disc,  $Q$ , is given by

$$Q(R) = -\frac{\dot{M}}{4\pi} \omega R \frac{d\omega}{dR} \left[ 1 - \frac{\omega(R_{ms}) R_{ms}^2}{\omega R^2} \right], \quad (A2)$$

where  $\omega$  is the rotation velocity. The colour temperature is given by,

$$qQ(R) = \sigma \left( \frac{T}{f_{col}} \right)^4, \quad (A3)$$

where  $\sigma$  is the Stefan-Boltzmann constant and  $q$  is the ratio of the disc flux to  $Q(R)$ , see equation (B6) below. When a fraction ( $f$ ) of  $Q(R)$  is dissipated in a corona above the disc surface (SZ94),  $q < 1$ , and the disc emission is due to both internal dissipation of  $(1-f)Q(R)$  and irradiation by the corona. We adopt the pseudo-Newtonian potential (Paczynski & Wiita 1980),

$$\Phi(R) = -\frac{GM}{R - 2R_g}. \quad (A4)$$

The rotation velocity is then

$$\omega(R) = \frac{1}{R - 2R_g} \left( \frac{GM}{R} \right)^{1/2}. \quad (A5)$$

Then we find from equations (A3)-(A2)

$$T(r) = T_0 \left[ \frac{r - 2/3}{r(r-2)^3} \left( 1 - \frac{3^{3/2} r - 2}{2^{1/2} r^{3/2}} \right) \right]^{1/4}, \quad (A6)$$

where  $r \equiv R/R_g$  and

$$T_0 = f_{col} \left( \frac{3\dot{M}qc^6}{8\pi\sigma G^2 M^2} \right)^{1/4}. \quad (A7)$$

At  $r \gg 6$ ,  $T(r) \simeq T_0 r^{-3/4}$ . The maximum  $T$  is

$$T_{max} = \begin{cases} c_0 T_0, & r_{in} < r_{max}, \\ T(r_{in}), & \text{otherwise,} \end{cases} \quad (A8)$$

where  $c_0 \simeq 0.1067$  and  $r_{max} \approx 9.505$ .

The (unscattered) flux emitted by the disc per unit photon energy,  $E$ , can be then obtained from equation (A1),

$$F_E = K E^3 \int_{r_{in}}^{\infty} \frac{r dr}{\exp[E/kT(r)] - 1}, \quad (A9)$$

where

$$K = (1 - p_{sc}) \frac{4\pi}{h^3 c^2} \left( \frac{GM}{c^2 D} \right)^2 \frac{\cos i}{f_{col}^4}, \quad (A10)$$

and  $h$  is the Planck constant. This model, under the name **diskpn**, is a part of the XSPEC packet. Its parameters are  $T_{max}$ ,  $r_{in}$  and the normalization,  $K$ .

From these parameters,  $M$  can be obtained from equation (A10), and then  $\dot{M}$  can be obtained using equations (A6)-(A8). For a constant  $K$ ,  $M \propto D f_{col}^2 \cos^{-1/2} i$ . For constant  $K$  and  $T_{max}$ ,  $\dot{M} \propto D^2 f_{col}^4 \cos^{-1} i$ . The disc luminosity is given by

$$L_s = \frac{2\pi D^2}{\cos i} \int F_E dE, \quad (A11)$$

which, for  $r_{in} = 6$ , equals

$$L_s = (1 - p_{sc}) q \frac{1}{16} \dot{M} c^2 = \frac{\pi \sigma G^2 M^2 T_{max}^4}{6 c_0^4 f_{col}^4 c^4}. \quad (A12)$$

Finally, we point out that the above model differs significantly from a commonly-used disc blackbody model, **diskbb** (Mitsuda et al. 1984) in XSPEC, in which the torque-free boundary condition is neglected and the asymptotic,  $r \gg 6$ , distribution is assumed, i.e.,  $T(r) = T_0 r^{-3/4}$ . This is a sufficiently accurate model for  $r_{in} \gg 6$ . However, when the disc extends close to the minimum stable orbit, the discrepancy between this  $T(r)$  and the  $T(r)$  of equation (A6) becomes very significant, as shown on Figure A1. Still, a **diskbb** spectrum can be made relatively accurate with some rescaling of  $R_{in}$  and  $T_{max}$ . We find in the case of  $r_{in} = 6$  that a PN spectrum at some  $R_{in}$  and  $T_{max}$  is close to the **diskbb** spectrum computed for  $R_{in}^{diskbb} \approx 2.73 R_{in}$  and  $T_{max}^{diskbb} \approx 1.04 T_{max}$ .

A more serious discrepancy regards the accretion efficiency. The efficiency ( $\eta \equiv L/\dot{M}c^2$ ) of a PN disc extending to the minimum stable orbit is  $\eta_{PN} = 1/16$ , very close to the exact value in the Schwarzschild metric,  $\eta_S = 1 - (8/9)^{1/2} \approx 0.0572$  (e.g. Kato, Fukue & Mineshige 1998), whereas the **diskbb** model yields  $\eta_{diskbb} = 1/4$ . Therefore,  $\dot{M}$  for discs extending to the minimum stable orbit computed using the **diskbb** model and assuming  $\eta_S$  (as sometimes done) is 4.37 times less than the actual  $\dot{M}$ .

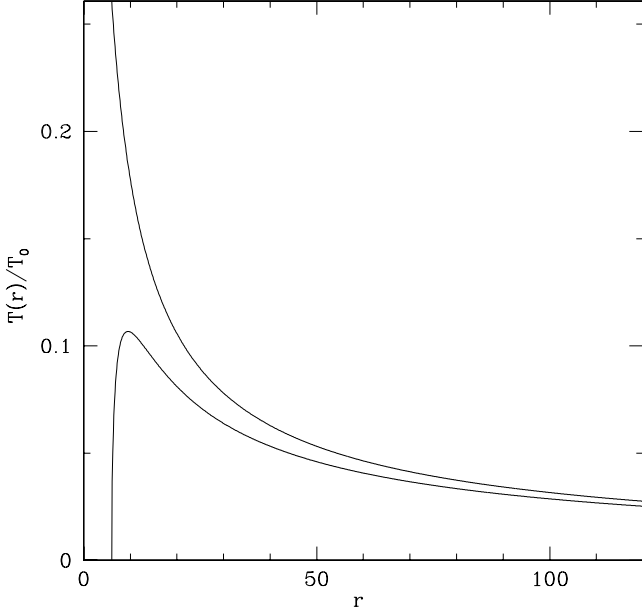


**Figure A1.** The radial temperature distribution in a pseudo-Newtonian disc, equation (A6) (lower curve) compared to the asymptotic distribution,  $\propto r^{-3/4}$ , used by the `diskbb` model (upper curve).

## APPENDIX B: ENERGY BALANCE IN DISC-CORONA SYSTEMS

We express here energy balance between a corona and an underlying disc (see Figure 6) in terms of the *observed* soft, hard and reflected fluxes,  $F_s$ ,  $F_h$  and  $F_r$ , respectively. This allows a direct comparison with results of data fitting, in which we can distinguish between the flux in unscattered disc photons ( $F_s$ ), the flux in scattered photons ( $F_h$ ), and the flux in the unscattered Compton-reflection and Fe  $K\alpha$  photons ( $F_r$ ).

We first note that  $F_s$  and  $F_h$  are related in different manners to the corresponding luminosities. The disc is optically thick and thus it radiates with a semi-isotropic specific intensity, which implies  $L_s = (2\pi/\cos i)D^2F_s$ . In general, the plasma emission can be anisotropic as well. If the emission radiated by the corona in directions away from the disc is isotropic (which we assume in this work),  $L_h = 4\pi D^2F_h$ .

We consider then a corona dissipating a fraction,  $f$ , of the total available power, with the underlying disc dissipating the remaining  $(1-f)$  fraction (SZ94). In general, the corona can be either homogeneous or patchy. In the latter case,  $L_s$  includes also emission of the part of the disc not covered by the corona. We will denote the powers dissipated in the corona and in the disc by  $P_c (= fL)$  and  $P_d [= (1-f)L]$ , respectively. From energy conservation,

$$L = P_c + P_d = L_h + L_s + L_r. \quad (\text{B1})$$

We will allow here for an anisotropic corona emission, in which the power emitted down equals  $d$  times the power emitted up. Also, we will include the power of Compton-reflected photons scattered in the corona in the total emission of the corona,  $(1+d)L_h$ . Thus, the total emission of the

corona includes its own dissipation and the power in photons emitted by the disc and then scattered,

$$(1+d)L_h = P_c + p_{sc}(P_d + dL_h), \quad (\text{B2})$$

where  $p_{sc}$  is the average probability of scattering of a photon emitted by the disc. This can be solved for

$$L_h = \frac{P_c + p_{sc}P_d}{1 + d(1 - p_{sc})}. \quad (\text{B3})$$

The luminosity in unscattered soft photons emitted by the disc includes parts due to the intrinsic disc emission and due to the reemission of the incident coronal emission,

$$L_s = (1 - p_{sc}) [P_d + d(1 - a)L_h] \quad (\text{B4})$$

(where  $a$  is the integrated albedo of the disc). The above equations can be solved for

$$L_s = \frac{(1 - p_{sc}) \{ [1 + d(1 - ap_{sc})] P_d + d(1 - a)P_c \}}{1 + d(1 - p_{sc})}. \quad (\text{B5})$$

The ratio of the soft flux at the disc surface to the total dissipation rate per unit area is

$$q = \frac{L_s}{(1 - p_{sc})L} \quad (\text{B6})$$

(see Appendix A). Finally, the luminosity in unscattered Compton-reflected photons is

$$L_r = (1 - p_{sc})daL_h. \quad (\text{B7})$$

The solution for  $f$  is

$$f = \frac{1 + d(1 - ap_{sc}) - p_{sc}(1 - p_{sc})^{-1}L_s/L_h}{1 + da(1 - p_{sc}) + L_s/L_h}. \quad (\text{B8})$$

We note that our results are consistent with those of Poutanen & Svensson (1996). However, their condition of energy balance is expressed in terms of the total soft emission of the disc (denoted by  $l_s$ ), which includes the part scattered in the corona, and the total emission of the corona ( $l_c$ ), which includes the (unobserved) coronal emission directed towards the disc surface. For comparison with observations, those quantities need to be transformed to the luminosities corresponding to observed fluxes; e.g.,  $l_c$  corresponds to  $(1+d)$  times the actual luminosity of the corona.

This paper has been produced using the Royal Astronomical Society/Blackwell Science  $\LaTeX$  style file.